

The receptor kinase SRF3 coordinates iron-level and flagellin dependent defense and growth responses in plants

Matthieu Platre

Salk Institute <https://orcid.org/0000-0002-4934-3050>

Santosh Satbhai

Indian Institute of Science Education and Research (IISER) Mohali <https://orcid.org/0000-0002-2770-656X>

Lukas Brent

Salk Institute

Matias Gleason

Salk Institute

Magali Grison

Laboratory of Membrane Biogenesis, UMR5200 CNRS, University of Bordeaux

Marie Glavier

university of Bordeaux <https://orcid.org/0000-0002-7100-7045>

Ling Zhang

Salk Institute

Min Cao

Salk Institute

Christophe Gaillochet

Salk Institute

Christian Göschl

Gregor Mendel Institute

Marco Giovannetti

Gregor Mendel Institute <https://orcid.org/0000-0003-4637-9880>

Balaji Enugutti

Gregor Mendel Institute (GMI), <https://orcid.org/0000-0002-0816-024X>

Marcel von Reth

Department of Plant-Microbe Interactions, Max Planck Institute for Plant Breeding Research

Rubén Alcázar

University of Barcelona

Jane Parker

Max Planck Institute for Plant Breeding Research <https://orcid.org/0000-0002-4700-6480>

Gregory Vert

Plant Science Research Laboratory (LRSV), UMR5546 CNRS/Université Toulouse 3

<https://orcid.org/0000-0002-0844-9991>

Emmanuelle Bayer

University of Bordeaux, CNRS, Laboratoire de Biogenèse Membranaire, UMR 5200 CNRS

<https://orcid.org/0000-0001-8642-5293>

Wolfgang Busch (✉ wbusch@salk.edu)

Salk Institute for Biological Studies <https://orcid.org/0000-0003-2042-7290>

Article

Keywords: plant growth responses, plant defence responses, iron, host-pathogen interactions

Posted Date: July 12th, 2021

DOI: <https://doi.org/10.21203/rs.3.rs-673556/v1>

License:   This work is licensed under a Creative Commons Attribution 4.0 International License.

[Read Full License](#)

Version of Record: A version of this preprint was published at Nature Communications on August 1st, 2022. See the published version at <https://doi.org/10.1038/s41467-022-32167-6>.

1 **The receptor kinase SRF3 coordinates iron-level and flagellin dependent defense and**
2 **growth responses in plants**

3
4 **Matthieu P. Platre¹, Santosh B. Satbhai^{1,2,3}, Lukas Brent¹, Matias F. Gleason¹, Magali**
5 **Grison⁴, Marie Glavier⁴, Ling Zhang¹, Min Cao¹, Christophe Gaillochet¹, Christian Goeschl²,**
6 **Marco Giovannetti², Balaji Enugutti², Marcel von Reth⁵, Ruben Alcázar⁵, Jane E. Parker^{5,6},**
7 **Grégory Vert⁷, Emmanuelle Bayer⁴, Wolfgang Busch^{1,2*}**

8 ¹ Salk Institute For Biological Studies, Plant Molecular And Cellular Biology Laboratory, 10010 N Torrey Pines Rd, La
9 Jolla, CA 92037, USA.

10 ² Gregor Mendel Institute (GMI), Austrian Academy of Sciences, Vienna Biocenter (VBC), Dr Bohr-Gasse 3, Vienna
11 1030, Austria.

12 ³ Department of Biological Sciences, Indian Institute of Science Education and Research, Mohali, Sector 8, SAS Nagar,
13 Punjab 14046, India

14 ⁴ University of Bordeaux, CNRS, Laboratoire de Biogenèse Membranaire, UMR 5200 CNRS, F-33140 Villenave
15 d'Ornon, France

16 ⁵ Department of Plant-Microbe Interactions, Max Planck Institute for Plant Breeding Research, Cologne, Germany.

17 ⁶ Cologne-Düsseldorf Cluster of Excellence on Plant Sciences (CEPLAS), 50225 Düsseldorf, Germany

18 ⁷ Plant Science Research Laboratory (LRSV), UMR5546 CNRS/Université Toulouse 3, 24 chemin de Borde Rouge,
19 31320 Auzesville-Tolosane, France.

20 *Correspondence: wbusch@salk.edu

21 **Iron is critical for host-pathogen interactions. While pathogens seek to scavenge iron to**
22 **spread, the host aims at decreasing iron availability to reduce pathogen virulence. Thus,**
23 **iron sensing and homeostasis are of particular importance to prevent host infection and**
24 **part of nutritional immunity. While the link between iron homeostasis and immunity**
25 **pathways is well established in plants, how iron levels are sensed and integrated with**
26 **immune response pathways remain unknown. We identified a receptor kinase,**
27 **SRF3 coordinating root growth, iron homeostasis and immunity pathways via regulation**
28 **of callose synthase activity. These processes are modulated by iron levels and rely on**
29 **SRF3 extracellular and kinase domain which tune its accumulation and partitioning at the**
30 **cell surface. Mimicking bacterial elicitation with the flagellin peptide flg22**
31 **phenocopies SRF3 regulation upon low iron levels and subsequent SRF3-dependent**
32 **responses. We propose that SRF3 is part of nutritional immunity responses involved in**
33 **sensing external iron levels.**

34
35 Iron is a critical micronutrient for all living organisms. While iron is very abundant in the Earth's
36 crust, its bioavailability is low. Organisms have evolved efficient iron uptake mechanisms that
37 include a variety of membrane-associated uptake systems that absorb iron unbound or bound to
38 iron-binding molecules. Mammals acquire iron mainly through the glycoprotein transferrin while
39 bacteria, fungi and plants have evolved diverse systems that include siderophores, which are
40 small, high-affinity diffusible secondary metabolites that chelate Fe³⁺ from the surrounding
41 environment¹. In plants, Graminaceae species employ plant specific siderophores while non-
42 Graminaceae such as *Arabidopsis thaliana* depend on an iron reduction-based uptake strategy².
43 During pathogen attack, iron is at the nexus of host-pathogen interaction as both organisms
44 compete for this metal. Pathogens scavenge iron from the host through siderophore secretion
45 while the host aims to sequester iron to prevent pathogen virulence. Thus, host external iron
46 sensing and internal iron homeostasis regulation are of particular importance to prevent pathogen
47 infection, and are part of the first line of defense called nutritional immunity³.

48 In mammals, two receptors, Transferrin Receptor 1 and 2 (TfR) which bind extracellular
49 transferrin-associated iron, play a major role in regulating external iron sensing and homeostasis.

50 Upon host-pathogen interaction, bacterial siderophores outcompete the host iron-bound to
51 transferrin, which in turn leads to a loss of iron triggering independent local and systemic
52 responses in the host⁴. Locally, the loss of iron induces TfR endocytosis and intracellular iron
53 storage via ferritins. Systemically, TfR activation triggers stimulation of the BMPR complex to
54 increase the expression of iron uptake genes⁴. The latter response is intertwined with defense
55 pathway since the inflammatory Interleukine-6 pathway directly interacts with the BMPR complex
56 to regulate iron uptake genes⁴. In *Drosophila melanogaster*, Transferrin-1 was recently shown to
57 activate NF- κ B, toll and immune deficiency immunity pathways, thereby mediating nutritional
58 immunity through the control of intracellular iron partitioning⁵.

59 Although flowering plants do not contain TfR in their genomes⁶, iron homeostasis and defense
60 responses are linked⁷. Here, FERRETINS (FER) and NATURAL RESISTANCE-ASSOCIATED
61 MACROPHAGE PROTEIN (NRAMPs) were shown to be involved in iron sequestration upon
62 pathogen attack^{8,9}. Moreover, the metal transceptor IRON-REGULATED TRANSPORT 1 (IRT1)
63 is critical to mount efficient defense responses¹⁰. Transcriptional signatures of *Pseudomonas*
64 *simiae* WCS417 and long-term iron deficiency in leaves display an overlap of about 20%, among
65 these genes, the transcription factor MYB DOMAIN PROTEIN 72 (MYB72) plays a role at the
66 interface of both signaling pathways¹¹⁻¹³. Recently, a protein effector from the foliar pathogen
67 *Pseudomonas syringae* was shown to disable a key iron homeostasis regulator, the E3 ligase
68 BRUTUS (BTS), to increase apoplastic iron content and promote colonization¹⁴. Finally, the
69 presence of the microbial siderophore, deferoxamine (DFO), affects the transcriptional
70 landscape of iron homeostasis and immunity genes, suggesting a role for siderophores in
71 mediating nutritional immunity¹⁰.

72 While the link between iron deficiency and immunity is well documented in plants, the mechanism
73 by which iron concentrations are sensed, and how they impinge on iron homeostasis, defense
74 and growth pathways are unknown. Here, we identify the leucine-rich repeats receptor kinase
75 STRUBBELIG RECEPTOR KINASE 3 (SRF3) through *Arabidopsis thaliana* natural root growth
76 variation under low iron levels using a genome wide association study (GWAS). We find that root
77 growth is rapidly reduced upon encountering low iron levels, that *SRF3* is required for this
78 response, and at the same time modulates root iron homeostasis. The regulatory capacity of
79 *SRF3* is dependent on its kinase and extracellular domains. Both domains are required for *SRF3*
80 partitioning between the plasmodesmata and the so-called bulk PM where it acts as a negative
81 regulator of callose synthases and is degraded upon low iron conditions in both sub-populations.
82 We further establish that *SRF3* is a molecular link between responses to low external iron levels
83 and bacterial defense responses, as *SRF3* is required to mediate root immune response to the
84 flagellin peptide flg22 by the same mechanisms used for its response to low iron conditions. Our
85 work uncovers a close coordination of responses to low iron levels and immunity pathways and
86 indicates that *SRF3* is located at the nexus of both pathways, thereby constituting a key player in
87 plant nutritional immunity.

88 89 **Results**

90 91 **SRF3 is a regulator of iron homeostasis genes and root growth under low iron levels**

92 Genome wide association studies (GWAS) for root growth rate under low iron levels revealed
93 multiple significantly associated single nucleotide polymorphisms (SNPs) (Figure S1A-B and
94 Spreadsheet S1). The most significant association was observed on chromosome 4 in close
95 proximity to the genes AT4G03390 (*STRUBBELIG-RECEPTOR FAMILY 3, SRF3*) and
96 AT4G03400 (*DWARF IN LIGHT 2, DFL2*) (Figures 1A). To identify potential causal genes at this
97 locus, we obtained Col-0 T-DNA mutant lines for these genes (Figures S1C-D) and quantified the
98 root growth response after three days exposure to low iron levels. While the *dfl2* T-DNA mutant
99 lines responded similarly to wildtype (WT) to low iron levels, *srf3* T-DNA lines displayed a
100 significantly decreased root growth response compared to WT when exposed to different iron

101 levels using the iron chelator Ferrozine (-FeFZ; 100, 50, 10 μ M; Figures 1B-C, S1E-G). Moreover,
102 *srf3* mutants showed a slight reduction in their root growth rate in iron sufficient conditions
103 compared to WT and responded similarly to WT to iron excess conditions (Figures 1C and S1G-
104 H). Overall, our data show that *SRF3* is required for an appropriate root growth response to low
105 iron levels.

106 To explore the function of *SRF3* on iron homeostasis genes, we performed RNAseq on roots from
107 two independent *srf3* alleles and WT under iron sufficient growth conditions. Several key iron
108 homeostasis regulators (*BTS*, *BHLH039*, *PYE*) and iron compartmentalization-related genes that
109 are involved in iron transport to the vacuole (*ZIF1*) were upregulated in *srf3* mutants while a key
110 iron distribution transporter involved in iron shoot-to-root partitioning was downregulated (*NAS4*;
111 Figure 1D and Spreadsheet S2). Consistent with a mis-regulation of iron responsive genes, the
112 transcriptional reporter line of the low iron inducible iron transporter *IRT1* (*pIRT1::NLS-2xYPet*) in
113 *srf3-4* mutant showed a decreased activation after 24 hours under low iron (Figure 1E). In line
114 with a misregulation of iron homeostasis, *srf3* mutants accumulate more iron compared to the
115 WT, thereby phenocopying *bts-1* and *opt3-2*, two iron homeostasis mutants known to accumulate
116 ectopic iron¹⁵⁻¹⁷ (Figures 1F and S2A-C). Importantly, the increased iron levels in *srf3-3* do not
117 stem from increased iron content in the seeds since the iron localization was not altered in *srf3*
118 mutant seeds compared to WT but different from *vit-1* embryos that are known for misdistribution
119 of iron¹⁸ (Figure S2D). Taken together, these results indicate that *SRF3* is a post-embryonic
120 regulator of iron homeostasis genes.

121 Next, we investigated the allelic variation at the *SRF3* locus and analyzed accessions according
122 to the pattern of the four top marker polymorphisms associated with the growth response under
123 low iron conditions. The four resulting groups of accessions were haplogroup A that grows slowly
124 on low iron medium and the haplogroups B, C, D that grow faster (Figures S3A-C). While the
125 haplogroup A and haplogroup B differed from several candidate polymorphisms including a larger
126 deletion in the promoter region (Figure S3A), they do not show any significant differences in *SRF3*
127 transcript level accumulation under low iron levels (Figure S3D-E). These results highlight that
128 *SRF3* allelic variation does not lead to obvious changes in *SRF3* transcript levels in bulk root
129 tissue, showing no correlation with the observed variation of root growth rates in low iron
130 conditions. Taken together, our data show that *SRF3* is a negative root growth regulator under
131 low iron levels and is involved in the post-embryonic regulation of iron homeostasis, a function
132 which might be independent of its expression levels.

133 134 **The early growth response to low iron is dependent on SRF3 protein levels at the plasma** 135 **membrane**

136 *SRF3* encodes a gene belonging to the protein family of leucine-rich repeats receptor kinases
137 (LRR-RKs) which are known to be involved in early signal transduction¹⁹. We hypothesized that
138 *SRF3* might mediate a novel, immediate root response to changes in external iron levels. Using
139 live-light transmission microscopy for 12 hours, we found that low iron levels elicited a significant
140 decrease of root growth after 4 hours and that this response was abolished in *srf3-3* (Figures 2A,
141 S4A and Movie S1-2). The cause of this unresponsiveness in *srf3* is partly explained by a lack of
142 cell elongation decrease upon low iron conditions (Figures S4B-F). To further investigate the role
143 of *SRF3* in regulating root elongation under low iron, we monitored the response of *SRF3*
144 transcription and SRF3 protein abundance using transcriptional and translational reporter lines.
145 A SRF3-2xmCHERRY fusion construct driven by its own promoter fully complemented the *srf3-3*
146 root growth defect under low iron levels, showing the functionality of the construct (Figure S1F
147 and S4G). The transcriptional reporter line revealed that the *SRF3* promoter is active in the
148 differentiation and elongation zones, and to a lesser extent in the transition zone (Figures 2B).
149 Surprisingly, the SRF3 fluorescent protein fusion was detected mainly at the PM in the apical and
150 basal meristem and to a lesser extent in the transition, elongation and differentiation zones
151 (Figures 2B). We confirmed this finding in Landsberg *erecta* (Ler) WT background using a GFP

152 tag fused to the respective full genomic fragment (Figure S4H-L). We reasoned that the SRF3
153 protein and/or transcript might be cell-to-cell mobile, or that the *SRF3* transcript might expressed
154 transiently in the meristematic cells. Analysis of numerous root tips showed that some roots
155 expressed the *SRF3* transcriptional reporter in the meristematic zone, a finding backed up by
156 single cell sequencing data, however, we could not exclude the alternative hypothesis²⁰ (Figure
157 S4M-P). Overall, *SRF3* is constantly transcribed and translated in the transition-elongation zone
158 and transiently or only in a subset of cells in the meristematic zone.

159 We next tested whether SRF3 protein abundance or *SRF3* transcription are altered in response
160 to low iron conditions in the transition-elongation zone. While the signal intensity in the *SRF3*
161 transcriptional reporter line did not differ between the two iron regimes, similarly to the control line
162 H2B-mSCARLET, the fluorescent signal intensity in a reporter line in which SRF3 was driven by
163 *UBIQUITIN10* promoter (*SRF3*^{WT}) or its native promoter significantly decreased at the PM under
164 low iron treatment compared to the Lti6b-GFP control line (Figures 2D and S5A-B). Time lapse
165 analysis showed that a signal decrease was recorded after 50 minutes in *SRF3*^{WT} but not in the
166 other lines (Figures 2C, Movies S3, S4 and S5). We next set out to dissect the role of the functional
167 domains of SRF3 for this process and generated a truncated version of SRF3 in which the
168 extracellular domain had been removed (*SRF3*^{ΔExtraC}) and a kinase dead version, containing a
169 mis-sense mutation in a critical residue in the catalytic ATP binding pocket (*SRF3*^{KD}, Figures S5C-
170 D). While the functional SRF3 protein levels were decreased (*SRF3*^{WT}) after two hours of
171 exposure to low iron conditions, this was not observed for the *SRF3*^{ΔExtraC} or *SRF3*^{KD} lines (Figure
172 2D). This shows that both, the extracellular cellular domain and kinase activity are required to
173 mediate the decrease of SRF3 protein at the PM in response to low iron levels.

174 We then investigated whether SRF3 levels control early root growth rate under low iron conditions.
175 Surprisingly, much like SRF3 loss of function, constitutive expression of SRF3 abolished the early
176 root growth response to low iron levels (Figures 2E). However, we observed an opposite effect in
177 *srf3* mutant and *SRF3*^{WT} overexpressing plants during the late response to low iron (Figure S5E).
178 Although this complex response is yet to be fully explained, we used this property to interrogate
179 SRF3 domain functions. To do so, we investigated the early growth response of the
180 overexpressing lines of *SRF3*^{ΔExtraC} (*pUBQ10::SRF3*^{ΔExtraC}-*mCITRINE*), *SRF3*^{KD}
181 (*pUBQ10::SRF3*^{KD}-*mCITRINE*) to low iron conditions. For both early and late low iron growth
182 responses, we observed that roots of *SRF3*^{ΔExtraC} and *SRF3*^{KD} presented a phenotype close to
183 WT, while the *SRF3*^{WT} version overexpressing line was hyposensitive or hypersensitive
184 respectively (Figures 2E and S5E). Altogether, our results suggest that the root growth response
185 to low iron conditions requires a fine regulation of SRF3 protein accumulation at the PM, which is
186 dependent on the extracellular and kinase domains. These findings are consistent with a model
187 in which SRF3 senses early apoplastic signals associated with iron depletion through its
188 extracellular domain and transduces the signal(s) intracellularly to modulate root growth via its
189 kinase activity.

190 191 **SRF3 resides in two subpopulations at the plasma membrane which are both decreased** 192 **under low iron conditions**

193 During the analysis of SRF3 expression, we had noticed its enrichment at the PM with a apical-
194 basal localization in punctate foci but also along the entire PM, referred to as bulk PM (Figures
195 S6A and S6C). We tested the role of its extracellular domain and kinase activity for specifying its
196 heterogenous distribution by calculating the standard deviation of the mean intensity (SDMI) along
197 the apical-basal side of PM using SRF3 truncated and point mutant versions. We found that
198 compared to the WT version, *SRF3*^{ΔExtraC} only associates with the bulk PM since we observed a
199 decrease of the SDMI (Figure 3A) while the removal of the kinase domain (*SRF3*^{ΔKinase}) did not
200 lead to SDMI changes (Figures S5C and S6B). This indicated that the extracellular domain is
201 necessary and sufficient to drive SRF3 into the PM-associated foci. Surprisingly, the standard
202 deviation of *SRF3*^{KD} fluorescent signal was significantly lower compared to *SRF3*^{WT} (Figures 3A),

203 suggesting a role of the kinase activity in SRF3 partitioning. We then investigated the role of SRF3
204 functional domains upon low iron levels. For SRF3^{WT}, a decrease of SDMI and polarity upon
205 exposure to low iron conditions were observed, indicating a loss of SRF3-associated punctate
206 structures while such reduction was not observed in the control line, LTI6b-GFP (Figure 3A and
207 S6C). Performing the same experiment with SRF3^{ΔExtraC} and SRF3^{KD} revealed no significant
208 difference upon low iron levels compared to the control condition (Figure 3A). This points to a role
209 of the extracellular domain and a requirement for an active SRF3 kinase in the removal of SRF3
210 from the foci upon exposure to low iron levels. Taken together, our data show that SRF3 has a
211 dual localization at the plasma membrane, in punctuated structures and the bulk PM that is
212 controlled by the extracellular domain and the kinase activity. Finally, upon exposure to low iron
213 levels, SRF3 seems to become less associated with the punctuated foci which also relies on its
214 functional domains.

215 We then addressed the nature of the PM-associated punctuated structures. Analysis of the
216 intensity distribution profile at the PM apical-basal sides of SRF3 fluorescent reporter in the
217 background of PM structure marker lines revealed a specific co-localization of SRF3 with
218 plasmodesmata-associated proteins CALS3 and PDLP3 but not the general PM marker Lti6b
219 (Figure 3B). Moreover, SRF3 co-localized with signals from Aniline blue staining that stains β-1,3-
220 glucan, which are particularly enriched in plasmodesmata (Figure S6D). This strongly indicated
221 that SRF3 localizes or is in close vicinity to the plasmodesma. To characterize and confirm SRF3
222 subcellular dynamics at higher resolution, we conducted immunogold labeling electron
223 microscopy of the *pSRF3::SRF3-GFP* line using an anti-GFP antibody. In standard conditions,
224 SRF3 signal was localized at the bulk PM and to the plasmodesmata and more specifically to the
225 plasmodesmatal neck region, and was removed not only from plasmodesmata but also the bulk
226 PM under low iron conditions (Figure 3C). As a recent report had shown that some
227 plasmodesmata-associated receptor kinases have a fast and reversible association between bulk
228 PM and plasmodesmata under abiotic stress, which alters their diffusion rates within the PM²¹,
229 we estimated SRF3 diffusion via fluorescence recovery after photobleaching (FRAP). We found
230 that a decrease of iron levels did not change SRF3 diffusion (Figure S6E), indicating that the
231 decrease of SRF3 is not accompanied by a change in its partitioning. Taken together, our data
232 indicate that SRF3 is associated with the bulk PM but also highly enriched at the neck of the
233 plasmodesmata, in an extracellular domain- and kinase activity-dependent manner. Under low
234 iron, SRF3 becomes depleted from these two subpopulations, a process which is dependent on
235 both SRF3 functional domains.

236

237 **Early lack of iron mediates SRF3-dependent callose deposition without affecting cell-to-** 238 **cell movement**

239 Immunogold-labeling electron microscopy suggested that SRF3 is particularly concentrated at the
240 plasmodesmata neck. This region is highly enriched in sterols, which are required for protein
241 targeting to this specific subregion to regulate plasmodesmata function²². Depleting plants
242 expressing SRF3^{WT} of sterols using sterol inhibitors, Fenpropimorph (Fen) and Lovastatin (Lova),
243 showed that SRF3 localization is sterols-dependent since a decrease of SRF3 polarity was
244 observed (Figures S7A), suggesting that SRF3 might have a functional role in this
245 plasmodesmata region. The plasmodesmatal neck is critical for regulating cell-to-cell trafficking,
246 as it is where callose turnover is thought to be regulated to determine plasmodesmata
247 permeability²³. Iron homeostasis depends on long- and local-distance signaling relying on cell-to-
248 cell movement to activate *IRT1*^{24–29}. We therefore hypothesized that SRF3 might regulate cell-to-
249 cell communication through callose turnover to properly activate *IRT1*. Analysis of signals from
250 immunostaining with a callose antibody indicated that low iron levels trigger callose deposition in
251 the epidermis and cortex cells of WT root tips (Figure 4A). This shows that iron levels influence
252 callose deposition. In *srf3* mutants, we observed an increase of callose even in the basal condition
253 while callose levels were not responsive to iron depleted media compared to WT (Figure 4A). Our

254 data therefore show that early responses to low iron include an increased callose deposition and
255 that SRF3 negatively regulates this process. To corroborate this finding, we used aniline blue to
256 quantify the signal in the epidermis of the root transition-elongation zone. The positive control, a
257 *CALLOSE SYNTHASE 3 (CALS3)* overexpressing line, which is known to accumulate ectopic
258 callose showed higher signal intensity compared to WT. In agreement with the antibody based
259 findings, low iron rapidly enhanced callose deposition in WT, however, increased callose was not
260 observed in WT when adding the 2-deoxy-d-glucose (DDG), a well-characterized callose
261 synthase inhibitor³⁰⁻³⁴. In *srf3* mutants, no difference in aniline blue signal intensity was observed
262 under iron sufficient conditions while an increase was observed under low iron compared to WT
263 in the same condition (Figure 4B). Although callose immunostaining and aniline blue slightly
264 differed, both experiments suggest that callose is synthesized by callose synthases shortly after
265 exposure to iron deficiency in an SRF3-dependent manner. Consistent with this conclusion, *srf3-2*
266 and *srf3-3* displayed fused LR and a higher LR density than WT, both of which are traits
267 associated with higher callose deposition (Benitez-Alfonso et al., 2013; Figures S7C-D).
268 We next investigated whether callose deposition upon low iron levels modifies cell-to-cell protein
269 movement in a SRF3-dependent manner. We first monitored the ability of GFP expressed in
270 companion cells using *pSUC2::GFP* to diffuse to the surrounding cells through the
271 plasmodesmata, as previously established³⁴⁻³⁶. Surprisingly, no difference in the GFP signal
272 distribution between WT and *srf3-3* root tips from plants grown on iron sufficient and low iron
273 containing media was observed (Figure 4C). To corroborate this observation, we photoactivated
274 DRONPA-s fluorescent protein in a single root epidermis cell and monitored its spread to the
275 upper and lower surrounding cells³⁷. We noticed a decrease of signal in the activated cell and a
276 concomitant increase in the surrounding cells, resulting from cell-to-cell movement. However and
277 consistent with our *pSUC2::GFP* observations, no difference between conditions and/or
278 genotypes was observed (Figure 4D). Altogether, our results suggest that a decrease of iron
279 levels swiftly leads to SRF3- and callose synthase-dependent modulation of callose deposition.
280 However, this does not generally impede cell-to-cell movement.

281 282 **Iron homeostasis and root growth are steered by SRF3-dependent callose synthases** 283 **signaling**

284 While *IRT1* activation is dependent on *SRF3*, this appears not to rely on a restriction of cell-to-
285 cell movement via callose synthases-mediated callose deposition during the early responses to
286 low iron conditions. We therefore reasoned that *IRT1* regulation might rely on early signaling
287 events that are dependent on callose synthases, or that *IRT1* regulation only occurs at a later
288 stage of the response. We first tested whether *IRT1* is regulated at the time during which SRF3-
289 dependent callose deposition occurs. A 16-hour time lapse analysis of *IRT1* promoter activity
290 indicated that the *IRT1* promoter becomes active during the first hours of low iron conditions while
291 no or little activity was observed in iron sufficient media (Figures 5A, Movie S6 and S7). In *srf3-4*
292 mutant roots, we observed a lower expression of the *IRT1* reporter line upon low iron conditions
293 compared to WT, indicating that early *IRT1* transcriptional activation depends on SRF3 (Figure
294 5B). Next, we tested whether callose synthases activity was important to activate *IRT1*
295 transcription by inhibiting callose synthases with DDG. The addition of DDG in low iron conditions
296 strongly reduced *IRT1* promoter activation in WT, which was not observed in the *srf3-4* mutant
297 compared to mock conditions (Figure 5B). All together, these observations indicate that *SRF3*
298 likely acts upstream of callose synthases-mediated signaling to ultimately tune the expression of
299 the major root iron transporter *IRT1*.

300 We next investigated the regulatory interaction of SRF3 and callose synthases by colocalization
301 analysis in roots using dual-color total internal reflection fluorescence (TIRF) revealing that SRF3
302 was organized in microdomains that partially colocalized with *CALS3* but not with the β -1,3-
303 glucanases reporter *PdBG1* known to negatively regulate callose deposition (Figure 5C). To test

304 these interactions genetically, we crossed *SRF3-OX*, which does not present any root growth
305 defects, with a mutated version of *CALS3* (*cals3-3d*) whose activity is up to 50% higher and
306 subsequently accumulates more callose, resulting in shorter roots than in WT³⁴. The double
307 homozygous lines of *SRF3-OXxcal3-3d* showed a further decrease of root growth compared to
308 the *cals3-3d* single mutant (Figures 5D and S7E), indicating a genetic interaction of SRF3 and
309 *CALS3*. To test whether the observed phenotype was due to a specific genetic interaction or a
310 more general interaction of increased callose levels and SRF3 overexpression, we used the
311 *35s::GFP-PDLP5* (*PDLP5-OX*) line, which presents similar callose and root growth phenotypes
312 as observed in *cals3-3d*^{38,39}. In this *SRF3-OXxPDLP5-OX* line, the root growth phenotype was
313 indistinguishable from the *PDLP5-OX* line, therefore highlighting the specific genetic interaction
314 of *SRF3* and *CALS3* (Figures 5D and S7E). Next, we set out to further test whether *SRF3* is acting
315 upstream or downstream of *CALS*s. We reasoned that if *CALS*s were upstream of SRF3, the
316 inhibition of callose synthase activity would impact SRF3 PM levels. Co-treatment of low iron with
317 DDG did not modify PM-associated SRF3 levels and therefore suggested that callose synthase
318 is downstream of SRF3 (Figure S7F). This finding was corroborated by monitoring the early and
319 late root growth rate of WT and *srf3-3* during the application of DDG and low iron levels as a
320 partial complementation of *srf3-3* root growth phenotype was observed in that condition (Figures
321 5E and S7G). Overall, our data suggest that SRF3 acts upstream of the callose synthase early-
322 on upon low iron levels to regulate iron homeostasis and root growth.

323

324 **SRF3 coordinates iron homeostasis and bacteria elicited immune responses**

325 *SRF3* was originally identified as a genetic locus underlying immune-related hybrid incompatibility
326 in *Arabidopsis* and shown to be involved in bacterial defense-related pathways in leaves (Alcazar
327 et al., 2010). Gene ontology (GO) analysis of root RNAseq data in standard condition and the
328 analysis of the root specific *pCYP71A12::GUS* immune reporter upon treatment with the bacterial
329 elicitor flg22 showed that SRF3 has a similar role in roots⁴⁰ (Figure 6A and S8A). We then
330 investigated the specificity of SRF3's role by assessing the late root growth responses to different
331 pathogen-associated molecular patterns (PAMPs) and plant-derived damage-associated
332 molecular patterns (DAMPs). *srf3* roots were only impaired in their response to flg22 but not to
333 chitin or AtPep1 compared to WT (Figures S8B-C). Similar to the low iron level response, the
334 flg22 response was already apparent early-on in WT and absent in *srf3* mutants (Figures 6B,
335 S8D-E and Movies S8, S9). To test whether the increased iron content of *srf3* might be related to
336 this response, we analyzed the early and late root growth responses to flg22 of *bts-1* and *opt3-2*.
337 They both responded like WT, indicating that higher iron root content does not generally affect
338 the root growth regulation upon immune response elicitation^{16,17} (Figures S8F-H). We therefore
339 concluded that the role of *SRF3* in controlling early root growth upon bacterial elicitation is specific
340 and related to its signaling activity.

341 Because of the similar growth response to low iron levels and flg22 treatment, we hypothesized
342 that the SRF3-dependent root growth regulation to these two stresses might rely on the similar
343 molecular mechanism. Consistent with this idea, we found that upon flg22 treatment, the SRF3
344 protein displays similar cellular dynamics as observed under low iron conditions (Figure 6C and
345 S8I) while no significant changes of SRF3 transcriptional regulation were observed (Figure S8J).
346 Therefore, SRF3 appears to be a point of convergence between iron and flg22-dependent
347 signaling mediating root growth regulation.

348 We reasoned that one model explaining this convergence is that flg22 might trigger a transient
349 decrease of cellular iron levels, thus promoting SRF3 degradation. We therefore performed
350 RhoNox-1 staining after 1 hour of flg22 treatment and observed a decrease of fluorescence
351 compared to mock treatment (Figure 6D). This indicates a swift decrease of local iron
352 concentration in roots upon flg22 stimulus. Consistent with a rapid decrease of cellular iron, flg22
353 treatment rapidly enhanced *IRT1* expression (Figure 6E, S9A and Movie S10). Moreover, mining
354 of publicly available root RNAseq data revealed a broad impact of short-term flg22 treatment on

355 the expression of iron homeostasis genes (Spreadsheet S3; Stringlis et al., 2018). We then
356 wondered whether the flg22-triggered iron deficiency responses rely on SRF3-dependent callose
357 synthase activity. Co-treatment of WT roots with DDG and flg22 led to a decrease of *IRT1*
358 promoter activity compared to flg22 treatment alone, while in *srf3-4* this activation was decreased
359 under flg22 compared to WT and insensitive upon co-treatment (Figure 6E). Overall, these data
360 indicate that flg22-dependent *IRT1* activation relies on SRF3-mediated callose synthase signaling
361 as observed for low iron conditions.

362 Finally, to investigate the extent of *SRF3*-dependent coordination of bacterial immune responses
363 and iron homeostasis, we performed an RNAseq analysis after two hours of exposure to low iron
364 levels or flg22 in *srf3* mutant and WT roots. Strikingly, 90% of the differentially expressed genes
365 (DEGs) in these two conditions overlapped and were up or down regulated in the same manner
366 in WT. Importantly, these DEGs were not associated with a general stress response since none
367 of these common iron and flg22 DEGs were overlapping with those in cold, NaCl and mannitol
368 datasets⁴² (Figure 6F, S9B and Spreadsheet S4 and S5). To further confirm that low iron levels
369 trigger immunity genes, we conducted qPCR for two early markers of flg22-triggered immunity,
370 *FRK1* and *MYB51* that showed a transient activation of the two genes within four hours (Figure
371 S9C; He et al., 2006). To determine how much of this common transcriptional program is
372 coordinated by SRF3, we analyzed the *srf3* transcriptome datasets. DEGs in flg22 and iron
373 deficiency in *srf3* mutant roots only overlapped by 24% demonstrating that *SRF3* coordinates a
374 large part of the common transcriptional program that is triggered in response to early response
375 to low iron and to flg22 (Figure 6F). Overall, our work establishes SRF3 as a major coordinator of
376 bacterial immune response and iron deficiency signaling pathways which relies on callose
377 synthase signaling.

378 **Discussion**

379 Based on a GWAS approach, we have identified an LRR-RK, *SRF3* as a regulator of early root
380 growth responses to low iron conditions. We show that SRF3 transduces signals that lead to a
381 coordinated response of root growth regulation, iron homeostasis and bacterial immunity through
382 its modulation of callose synthase-dependent signaling. Because this is highly reminiscent of
383 nutritional immunity conferred by the TfR mammalian and *Drosophila* systems that sense iron
384 levels and control iron and immune responses, we propose that *SRF3* is instrumental in mediating
385 plant nutritional immunity^{3,5}.

386
387 We discovered that root growth is modulated within the first four hours upon exposure to low iron
388 levels looking at earlier time points than usually considered^{16,24,44,45} (Figure 2A). This early
389 response is SRF3-dependent, exposing this LRR-RK as being a key part of the genetically
390 encoded ability of roots to perceive and transduce low environmental iron levels. A
391 comprehensive SRF3 domain characterization showed that the LRR and the kinase activity are
392 critical not only for its organization at the PM but also to mediate SRF3 decrease-dependent root
393 growth arrest under low iron (Figure 2). In light of other LRR-RK signalling transduction
394 mechanisms, such as those for BRI1 and FLS2^{19,46-48}, our results lead towards the following
395 model for SRF3 1) the LRR extracellular domains senses a signal that is informative of the early
396 lack of iron, 2) which in turn activates the kinase activity 3) which then triggers decrease of its
397 level at the PM, 4) to regulate early root growth. We also found that the role of SRF3 in transducing
398 low iron levels at an early stage is not restricted to the root growth regulation according to the
399 RNAseq analysis (Figure 1E, 5B and 6). However, we did not provide direct evidence of the
400 involvement of SRF3 kinase activity and LRR in transducing signals to regulate iron homeostasis
401 and bacterial immune pathways. However, this is very likely since SRF3 is known to be part of
402 the phosphorelay upon PAMP immune response⁴⁹. Much of the *SRF3* function is tied to the SRF3
403 signal transduction because no obvious changes in SRF3 transcriptional level in flg22 or low iron
404 treatments were observed (Figures S5A and S8J), and no correlation between the expression
405

406 level of *SRF3* in accessions that displayed contrasting root growth responses to low iron levels
407 were observed (Figure S3E). Yet, an early or cell-type specific *SRF3* transcriptional regulation
408 cannot be excluded. Altogether, our data indicate that roots perceive external variation of iron
409 rapidly through *SRF3*-dependent signal transduction to coordinate root signaling pathways.

410
411 We have found that *SRF3* acts upstream of iron-induced callose synthases activity to mediate
412 proper signaling. Aniline blue and immunostaining showed that the early low iron response goes
413 along with callose synthase-dependent callose deposition. Even though, these two techniques
414 indicated conflicting results for callose deposition levels in the basal condition in WT and *srf3-3*,
415 which might be explained by technical reasons, both approaches pinpointed *SRF3* acts as
416 negative regulator of this process (Figures 4A and 4B). The role of *SRF3* acts as an upstream
417 negative regulator of callose synthases is further strengthened by several lines of evidence: *SRF3*
418 and *CALS3* colocalize in both *SRF3* PM subpopulations (Figure 3B and 5C), genetically act in the
419 same pathway and the root growth response to low iron levels of *srf3* mutants is partially
420 complemented upon inhibition of callose synthases (Figure 5B-E). Surprisingly, cell-to-cell
421 movement of proteins were not affected early-on upon low iron levels, despite callose synthases
422 activation and increased callose deposition in the plasmodesmata (Figure 4C-D). However, it is
423 possible that callose deposition might impact later responses since callose deposition-mediated
424 plasmodesmata closure can take hours to days to occur^{38,50-53}. Another possibility is that callose
425 deposition might have a different function early-on, for instance early ROS signaling which is
426 thought to mediate callose deposition, actually increases cell-to-cell communication in leaves⁵⁴.
427 Thus, even though root growth, iron homeostasis and defense signaling can be controlled by cell-
428 to-cell movement of signaling molecules movement, *SRF3* dependent regulation of these
429 pathways doesn't rely on impeding cell-to-cell movement thereby putting the spotlight onto a
430 signaling function of callose synthases. In line with this idea, the double mutant *SRF3-OX/cals3-*
431 *3d* displayed shorter roots compared to *cals3-3d* which should in fact show longer roots if *SRF3*
432 was strictly restricted to its repressive role on callose deposition (Figures 5D). Taken together, we
433 have found that *SRF3*-dependent callose synthase activity is required to regulate early root
434 growth, iron homeostasis and defense signaling pathways under low iron levels, which might
435 dependent directly on callose synthase-mediated signaling rather than impeding cell-to-cell
436 movement.

437
438 We have found that *SRF3*-mediated signaling is at the nexus of the early root responses to low
439 iron and bacterial-derived signal. In fact, RNAseq analysis revealed that early responses to low
440 iron and flg22 are highly similar and largely coordinated by *SRF3* (Figure 6F). The axis of *SRF3*
441 and callose synthases is of particular importance for the regulation iron homeostasis genes in
442 both conditions as revealed by monitoring *IRT1* promotor activity (Figure 5B and 6E). The local
443 and swift decrease of iron in the root upon flg22 treatment might be the mechanism that underlies
444 the flg22 dependent activation of iron homeostasis genes (Figure 6D-C). Conversely, the early
445 lack of iron is able to activate the PTI signaling pathways, which is also mediated by *SRF3*
446 (Figures 6F and S9C). This activation of PTI signaling upon low iron levels is likely due to *SRF3*'s
447 role to modulate iron homeostasis which is important to coordinate immune responses^{7,13} (Figures
448 1D-E and 5B Spreadsheet S2). However, there is an alternative model that cannot be excluded.
449 In this model *SRF3* regulates flg22-mediated PTI signaling pathways, which in turn modulates
450 iron homeostasis. This model is in line with the specific *SRF3*-dependent root growth regulation
451 under flg22, the RNAseq data from *srf3* mutant roots in which PTI-dependent genes are
452 misregulated (Spreadsheet S2, S4 and Figure S9D) and experimental data provided in
453 Smakowska-Luzan et al., 2018, based on the extracellular network. Further supporting this
454 hypothesis, we found that the early and late root growth responses of *fls2* mutants, which are
455 impaired in PTI-triggering immunity are decreased under low iron levels (Figure S9E-
456 H). Altogether, our observations lead to a model in which *SRF3* perceives an early lack of iron to

457 modulate iron homeostasis and PTI signaling pathways, however it remains to be investigated
458 which pathway is upstream of the other.

459
460 During host-pathogen interactions, an early host line of defense is to withhold iron to limit
461 pathogen virulence, which is part of the nutritional immune responses as previously reported in
462 vertebrates and invertebrates^{4,5}. Eliciting bacterial immune responses triggers a SRF3-dependent
463 decrease of cellular iron levels, showing a conserved principle of this nutritional immune response
464 being present in plants (Figures 1F and 6D). In line with this idea, we have found that the lack of
465 *SRF3* impedes mechanisms relating to the ability of root tissues to withhold iron. For instance,
466 *ZIF1* that is involved in iron storage in the vacuole is upregulated in *srf3* mutants, while *NAS4* that
467 is involved in root-to-shoot iron transport is downregulated^{56,57} (Figure 1D; Spreadsheet S2). In
468 parallel, *NAS4* modulates ferritin accumulation, which is another way for the plant to withhold
469 iron⁵⁸. Moreover, similar to the nutritional immunity systems described in mammals and
470 *Drosophila melanogaster* that are based on TfR, SRF3 senses the immediate lack of iron which
471 is also relayed to a common signaling pathway linking iron deficiency and immunity responses³
472 (e.g. BMPR; Figure 6F). Altogether, we therefore propose that SRF3 is a central player in a
473 mechanism that embodies a fundamental principle of nutritional immunity by coordinating
474 bacterial immunity and iron signaling pathways via sensing iron levels.

475
476
477 **Acknowledgements:** We thank Y. Belkhadir, B. Lacombe, I. Helariutta and all the Busch lab
478 members for critical discussions. Y. Jaillais for sharing cloning materials, F. Berger for providing
479 H2B in PDONR P1P2, J.B.D Long for providing SV40, Y. Benitez-Alfonso for providing
480 35s:PdBG1-mCITRINE line, I. Helariutta for providing feedback on the manuscript and sharing
481 35s:GFP-CALS3 and *cals3-3d* as well as R. Stadler for providing 35s:DRONPA-s line. J.Y. Lee
482 for providing 35s::PDLP5-GFP line. E. Bayer for providing pPDLP3::PDLP3-YFP and
483 pSUC2::GFP lines. pCYP72A::GUS line was kindly provided by Y. Belkhadir. We thank, T. Zhang
484 and the Salk Biophotonics core team for microscopy advance and assistance in quantification.
485 We thank as well Salk peptide synthesis core especially Jill Meisenhelder and finally Br. Moussu
486 for thoughtful discussion. This study was funded by the National Institute of General Medical
487 Sciences of the National Institutes of Health (grant number R01GM127759 to W. Busch), a grant
488 from the Austrian Science Fund (FWF I2377-B25 to W. Busch), funds from the Austrian Academy
489 of Sciences through the Gregor Mendel Institute (W.Busch), and start-up funds from the Salk
490 Institute for Biological Studies (W. Busch). M.P. Platre was supported by a long-term postdoctoral
491 fellowship (LT000340/2019 L) by the Human Frontier Science Program Organization. R.A. and
492 J.E.P. were supported by The Max-Planck Society and Germany's Excellence Strategy CEPLAS
493 (EXC-2048/1, Project 390686111). M.v.R was funded by an IMPRS PhD fellowship. The
494 European Research Council (ERC) under the European Union's Horizon 2020 research and
495 innovation program (grant agreement No 772103-BRIDGING) to E. Bayer with the EMBO Young
496 Investigator Program to E. Bayer.

497
498 **Author contributions:** M.P. Platre was responsible of all experiments described in the
499 manuscript except for : qRT-PCR from extreme accessions performed by M. Giovannetti, B.
500 Enugutti did dry seed embryo dissection, Marcel von Reth, R. Alcazar and Jane E. Parker
501 generated and characterized the *pSRF3-SRF3-GFP* line, G. Vert provided pIRT1-NLS-2xYPET
502 line, S.B. Satbhai was involved in phenotyping, GWAS data processing and analysis, and
503 performing *pCYP72A11::GUS* experiment. C. Goeschl performed GWAS data plotting and GUS
504 signal quantification, L. Brent performed the selection and generation of transgenic lines, M.F.
505 Gleason imaged SRF3 reporter lines, M. Cao conducted qRT-PCR for immune genes under iron
506 deficiency, C. Gaillochet and L. Zhang performed RNAseq data analysis, M. Glavier performed
507 SRF3 immuno-gold electron microscopy and M. Grison performed callose immuno-localization.

508 M.P. Platre, S.B. Satbhai and W. Busch conceived the study and designed experiments. M.P.
509 Platre, W.Busch and E. Bayer wrote the manuscript, and all the authors discussed the results and
510 commented on the manuscript.

511

512 **Declaration of interest:** Authors declare no conflict of interest.

513

514

515

516

517

518

519

520

521

522

523

524

525

526

527

528

529

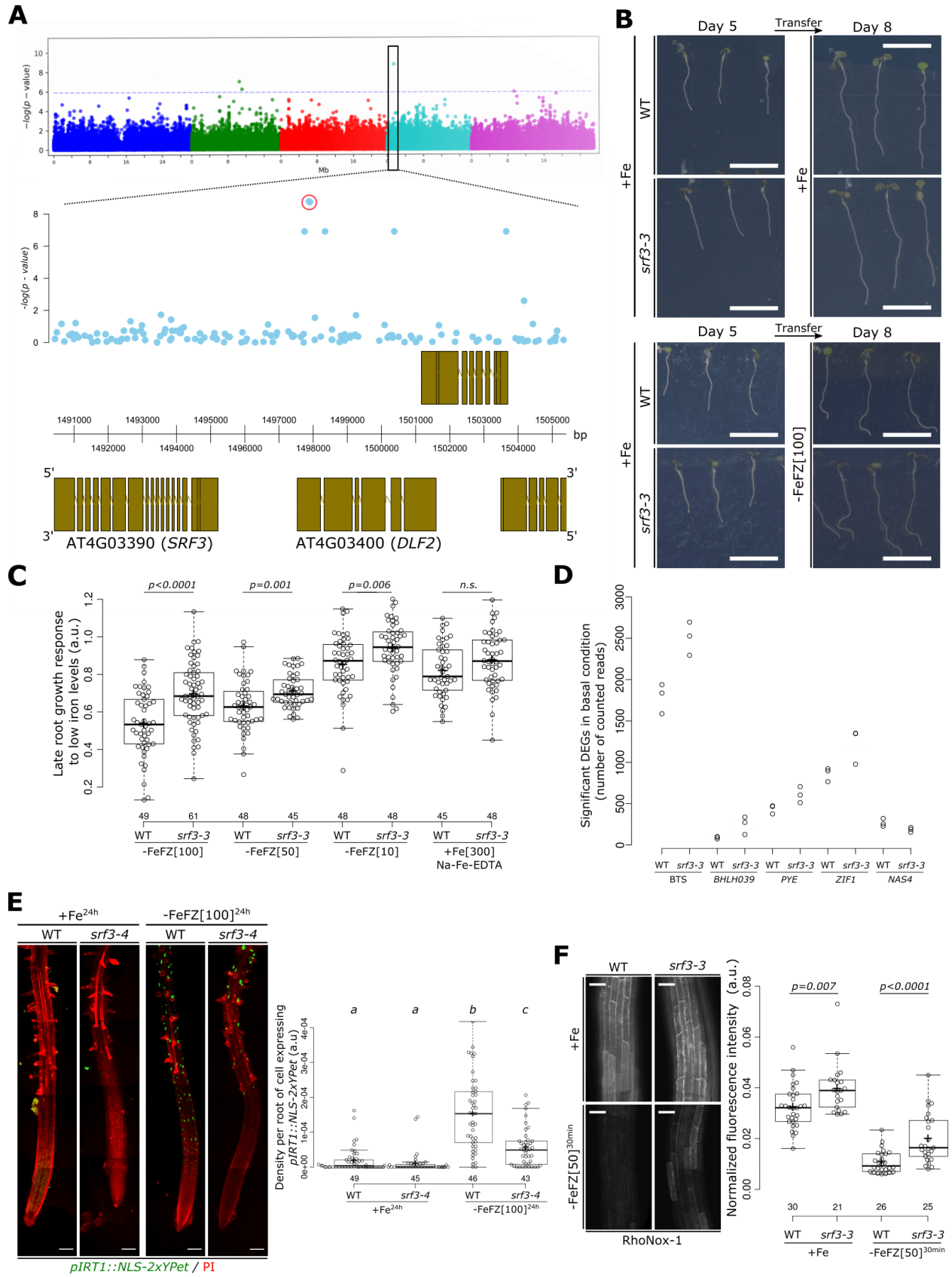
530

531

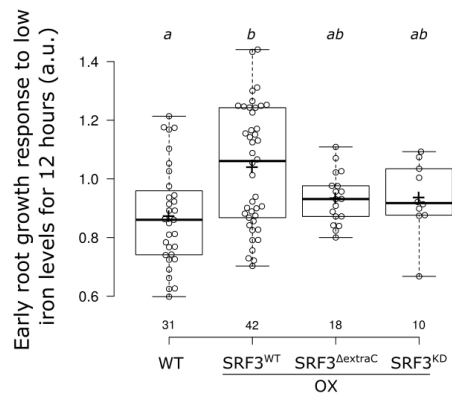
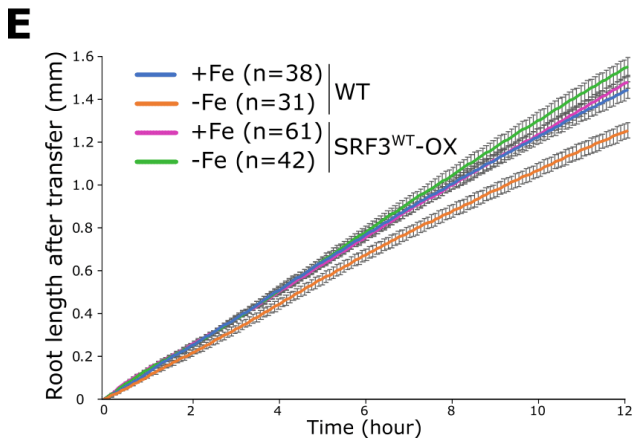
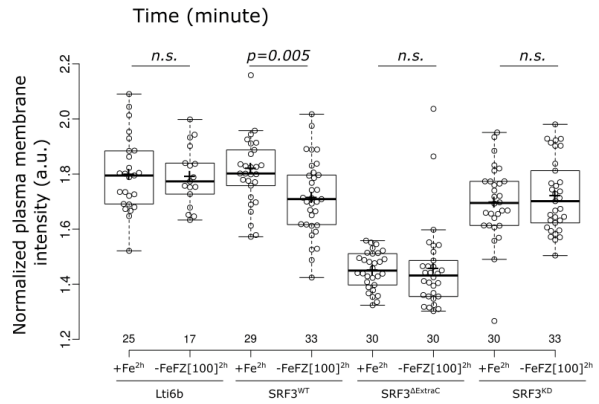
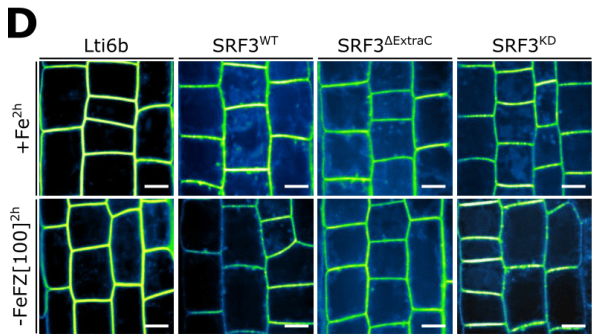
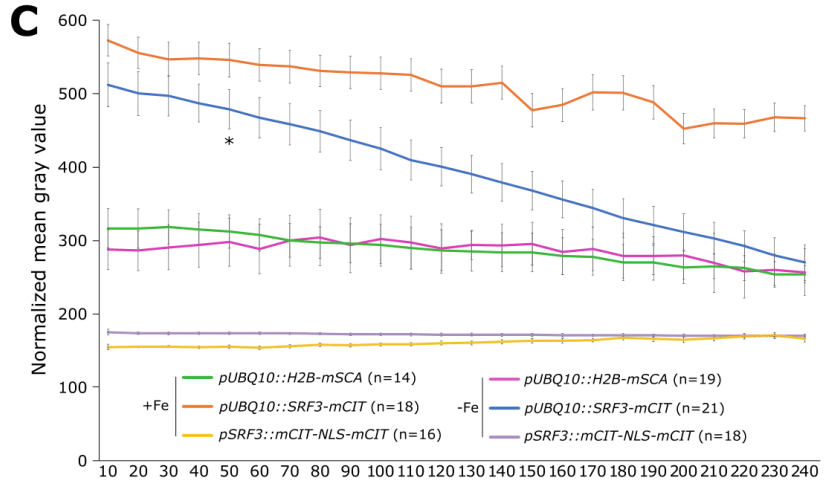
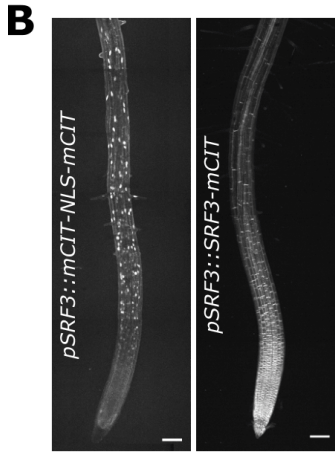
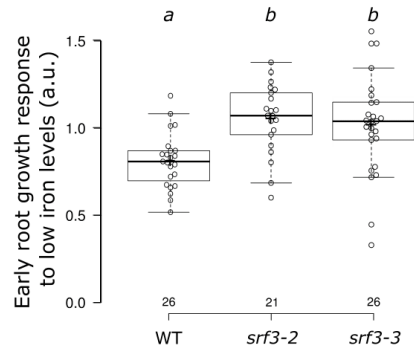
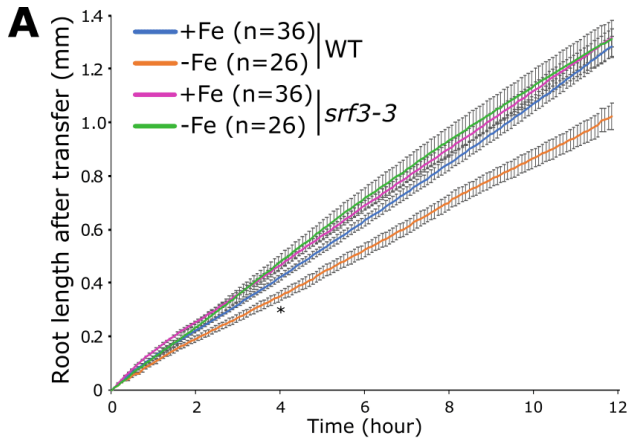
532

533

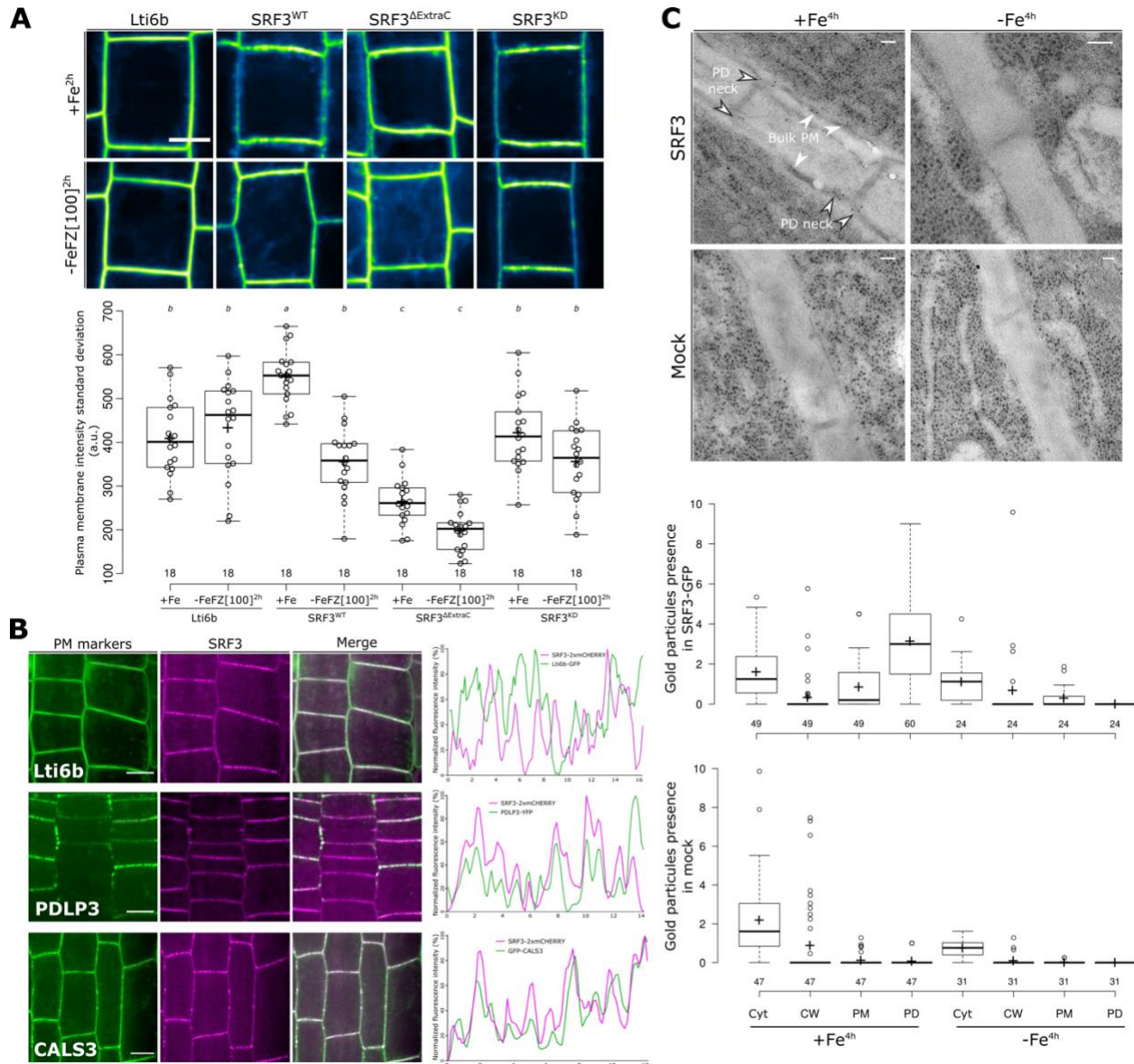
534



536 **Figure 1. SRF3 regulates root growth and iron homeostasis upon low iron conditions. (A)**
537 Upper panel: Manhattan plot for GWA mapping of the root growth rate day 4-5 of natural
538 accessions grown under low iron conditions. The horizontal dash dot line corresponds to a 5%
539 false discovery rate threshold. Black box indicates the significantly associated SNP that is in
540 proximity to *SRF3*. Lower panel: Magnified associations in the *SRF3* region with gene models.
541 **(B)** Representative images of 5 days old seedlings of WT and *srf3-3* under iron sufficient medium
542 for 5 days (left panel) and then transferred to iron sufficient media (+Fe; upper right panel), or to
543 low iron medium (-FeZ 100 μ M, lower right panel) and grown for 3 days. Scale bars, 1 cm. **(C)**
544 Boxplots of late root growth response to different iron levels (-FeZ 10,50,100 μ M or Na-Fe-EDTA
545 300 μ M) in WT and *srf3-3* seedlings [two-ways student test ($p < 0.05$), n.s. non-significant]. **(D)**
546 RNAseq read counts of differentially expressed iron homeostasis genes in roots of WT and *srf3-*
547 *3* in iron sufficient conditions. **(E)** 5 days old seedlings stained with propidium iodide (PI; red
548 channel) expressing *pIRT1::NLS-2xYPet* (green channel) in WT and *srf3-4* on sufficient (+Fe) or
549 low (-Fe) iron medium and the related quantification [one-way ANOVA follows by a post-hoc
550 Tukey HSD test, letters indicate statistical differences ($p < 0.05$)]. Scale bars, 100 μ m. **(F)** Confocal
551 images of 5 days old seedlings stained with RhoNox-1 in WT and *srf3-3* on sufficient medium
552 (+Fe; upper panel) or low iron medium (ferrozine 50 μ M, 30min; lower panel) and related
553 quantification [Independent two ways student test ($p < 0.05$)]. Scale bars 50 μ m.

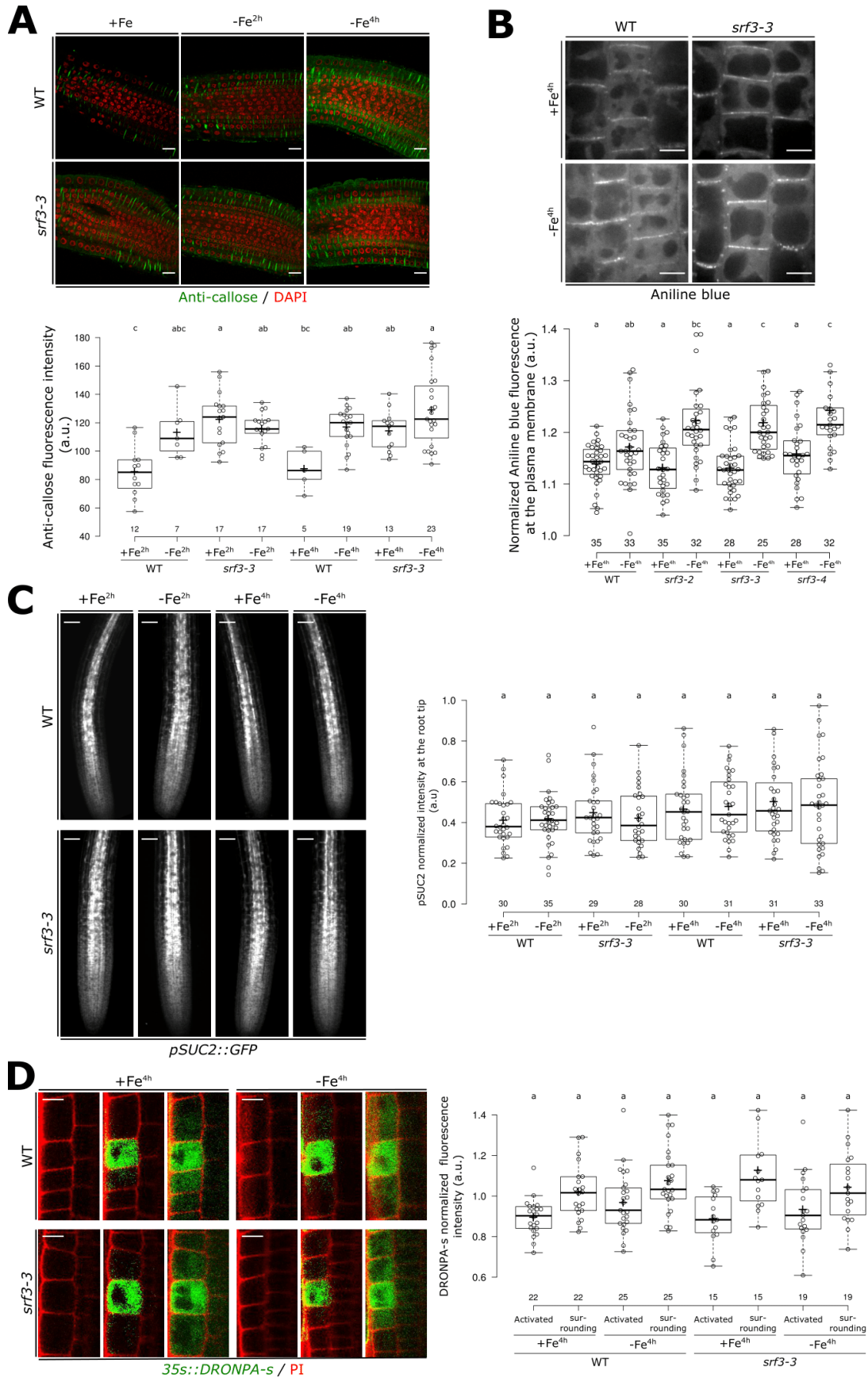


555 **Figure 2. SRF3 regulates early root growth response and undergoes for degradation**
556 **through its extracellular domain and kinase activity under iron deficiency. (A)** Graph
557 showing time lapse of the root length of WT and *srf3-3* under sufficient (+Fe) and low (-Fe) iron
558 medias [error bars: SEM; Asterix: significant difference between WT in +Fe and -Fe conditions
559 according to a mixed effect model ($p < 0.05$)] and the related quantification including the *srf3-2*
560 mutant [ANOVA with post-hoc Tukey test; Letters: statistical differences ($p < 0.05$)]. **(B)** Confocal
561 images of root tips of 5 days old seedlings expressing *pSRF3::mCITRINE-NLS-mCITRINE* and
562 *pSRF3::SRF3-mCITRINE*. Scale bars, 100 μ m. **(C)** Graph representing the fluorescence intensity
563 in the root tip of the indicated protein fusions under sufficient (+Fe) and low (-Fe) iron medias
564 [Asterix: significant difference between +Fe and -Fe for *pUBQ10::SRF3-mCITRINE* according to
565 a mixed effect model ($p < 0.05$)]. **(D)** Confocal images of 5 days old seedling expressing
566 *p35s::Lti6b-GFP*, *pUBQ10::SRF3^{WT}-mCITRINE*, *pUBQ10::SRF3 ^{Δ ExtraC}-mCITRINE*,
567 *pUBQ10::SRF3^{KD}-mCITRINE* under sufficient (+Fe, 2h) and low iron levels (-FeZ 100 μ M, 2h)
568 and the related quantification [two-ways student test ($p < 0.05$), n.s.: non-significant]. Scale bars
569 10 μ m. **(E)** Graph showing time lapse of the root length of WT and *SRF3^{WT}-OX* under sufficient
570 (+Fe) and low (-Fe) iron medias [error bars: SEM] and related quantification including *SRF3 ^{Δ ExtraC}*
571 and *SRF3^{KD}* [ANOVA with post-hoc Tukey test; Letters: statistical differences ($p < 0.05$)].

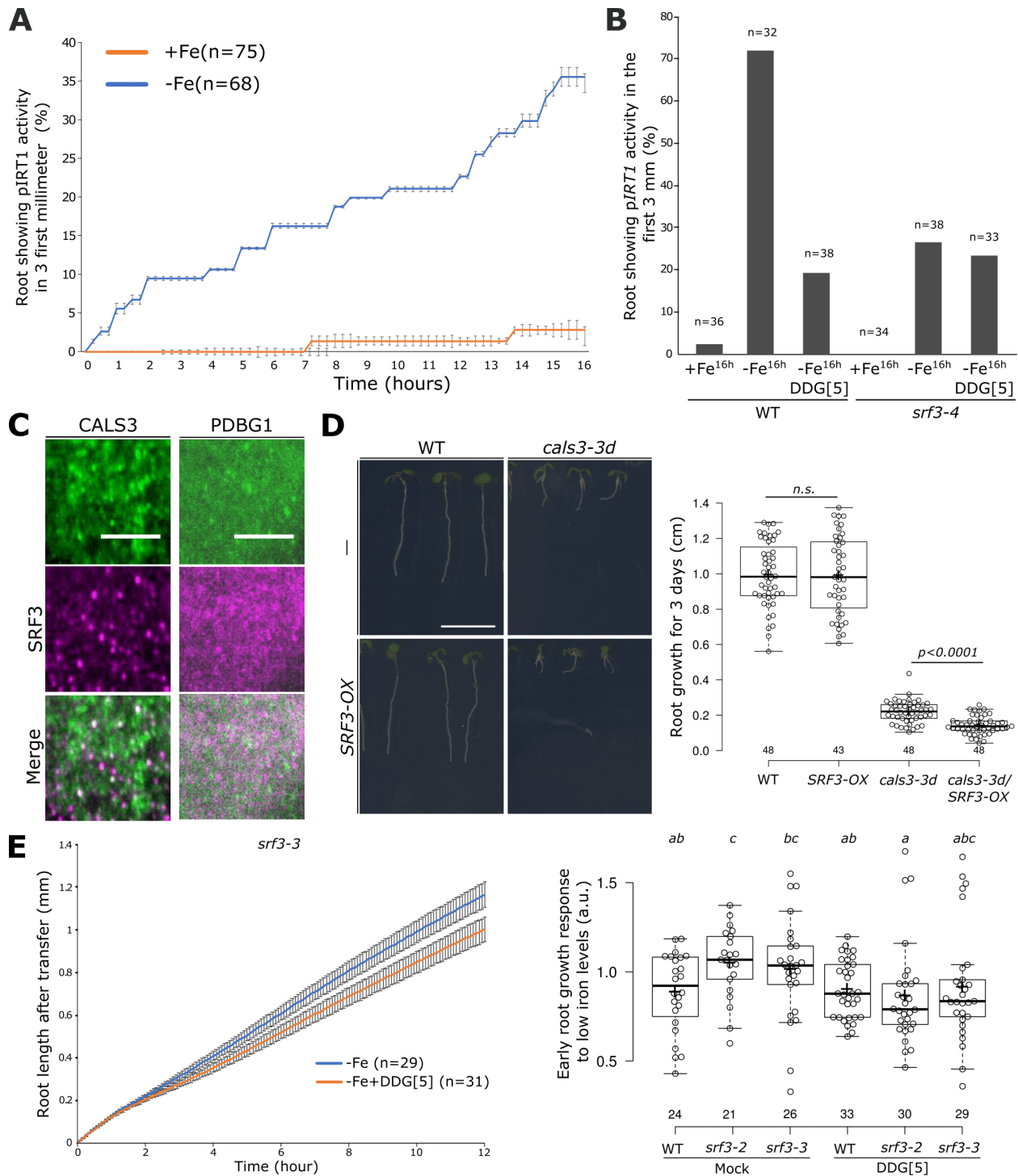


572
573
574
575
576
577
578
579
580
581
582
583
584
585
586
587

Figure 3. SRF3 co-exists in two subpopulations at the plasma membrane which decrease under low iron levels. (A) Confocal images of 5 days old seedling expressing *p35s::Lti6b-GFP*, *pUBQ10::SRF3-mCITRINE*, *pUBQ10::SRF3^{WT}-mCITRINE*, *pUBQ10::SRF3^{ΔExtraC}-mCITRINE*, *pUBQ10::SRF3^{KD}-mCITRINE* under iron sufficient (+Fe, 2h) or low iron (-FeZ 100μM, 2h) and the related quantification [ANOVA with post-hoc Tukey test; Letters: statistical differences (p<0.05)]. Note that the pictures have been pseudo-colored to emphasize changes in polarity and localization in the punctuated foci which does not reflect the proper fluorescence intensity. Scale bars, 10μm **(B)** Confocal images of 5 days-old seedlings co-expressing, *p35s::Lti6b-GFP*, *pPDLP3-PDLP3-YFP*, *35s::CALS3-GFP*, left, with *pUBQ10::SRF3-2xmCHERRY*, middle and the relative merge. Red line on the left image indicates where the scan line has been traced. Scale bars, 10μm. Right panel: graphs showing the signal intensity in both channel on the apical basal part of the cell. **(C)** Micrograph of immune gold with plant expressing *pSRF3::SRF3-GFP* (SRF3) and the relative control in *Ler* background under sufficient (+Fe, 4h) and low (-Fe, 4h) iron medias and the related quantification. Cyt, cytosol; CW, cell wall; PM, plasma membrane; PD, plasmodesmata. Scale bars, 100nm



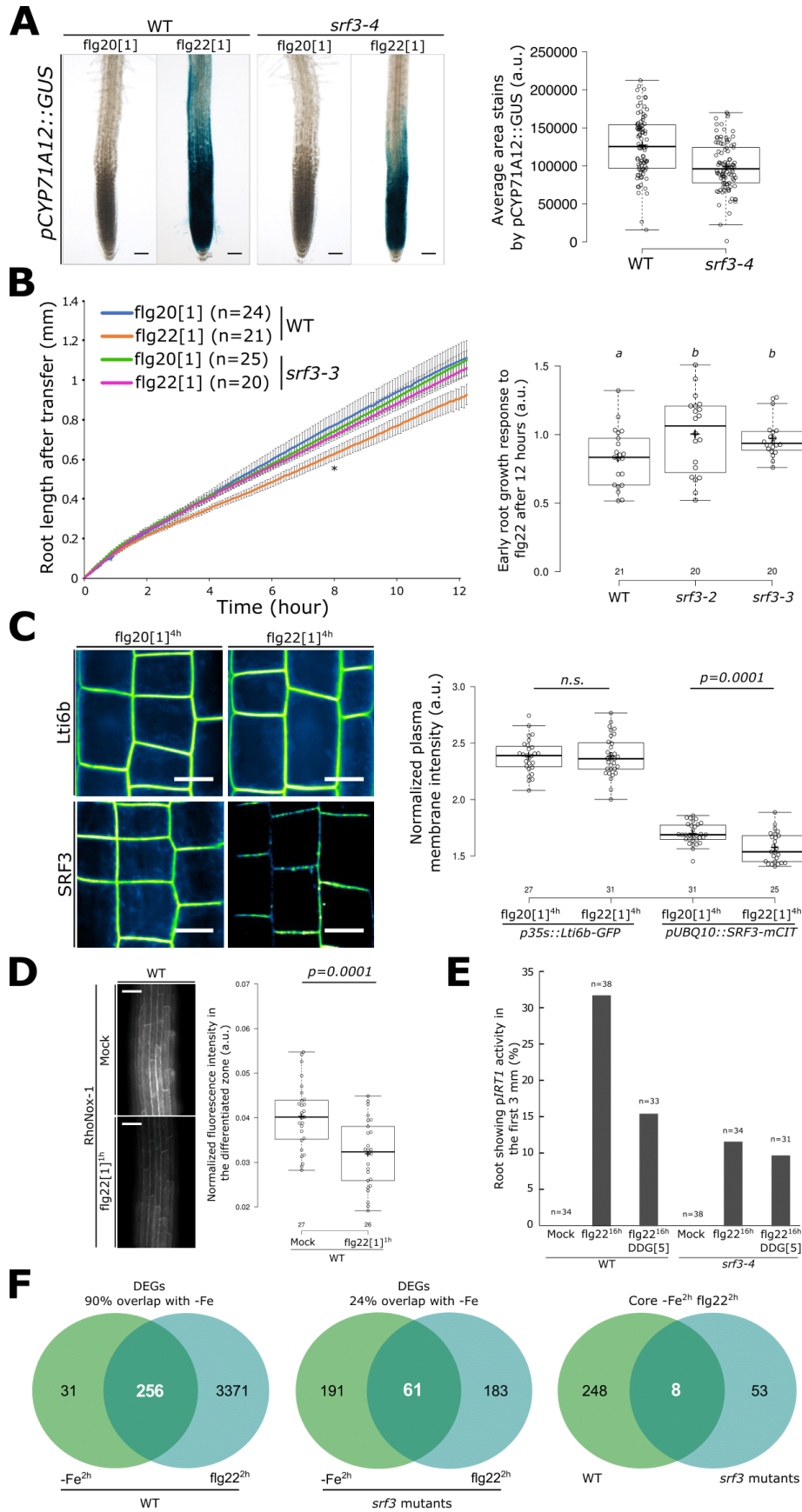
589 **Figure 4. SRF3 is a negative regulator of callose deposition but does not regulate cell-to-**
590 **cell signaling. (A)** Confocal images of root of 5 days old seedling stained with callose antibody
591 (green) and DAPI to stain the nucleus (red) under sufficient (+Fe, 2h and 4h) and low (-Fe, 2h
592 and 4h) iron medias and the related quantification [ANOVA with post-hoc Tukey test; Letters:
593 statistical differences ($p < 0.05$)]. Scale bars, 10 μ m. **(B)** Confocal images of 5 days old seedling
594 stained with aniline blue under sufficient (+Fe, 4h) and low (-Fe, 4h) iron medias in WT and *srf3-*
595 *3* and the related quantification [ANOVA with post-hoc Tukey test; Letters: statistical differences
596 ($p < 0.05$)]. Scale bars, 10 μ m. **(C)** Confocal images of 5 days old seedling expressing *pSUC2::GFP*
597 in WT and *srf3-3* under sufficient (+Fe) and low (-Fe) iron medias and the related quantification
598 [ANOVA with post-hoc Tukey test; Letters: statistical differences ($p < 0.05$)]. Scale bars, 50 μ m **(D)**
599 Confocal images of 5 days old seedling expressing *p35s::DRONPA-s* in WT and *srf3-3* under
600 sufficient (+Fe) and low (-Fe) iron medias and the related quantification [ANOVA with post-hoc
601 Tukey test; Letters: statistical differences ($p < 0.05$)]. Scale bars, 10 μ m.
602
603
604
605
606



607
608
609
610
611
612
613
614
615

Figure 5. Regulation of *IRT1* and root growth by SRF3-dependent callose synthase activity under low iron levels. (A) Graph representing the quantification of *pIRT1::NLS-2xYFPet* time lapse analysis under mock (+Fe) and low iron levels (-Fe) [error bars indicate SEM]. (B) Graph representing the percentage of root showing *IRT1* promoter activation under sufficient (+Fe, 16h) and low (-Fe, 16h) iron medias in WT and *srf3-4* in presence or absence of DDG. (C) Micrographs of 5 days old seedling expressing *35s::GFP-CALS3* (upper) and *UBQ10::SRF3-2xmCHERRY*

616 (middle) and merge channel (lower) in TIRF. Scale bars, 5 μ m. **(D)** Picture of 9 days old seedling
617 of WT, *cals3-3d*, *pUBQ10::SRF3-mCITRINE* (*SRF3-OX*) and *cals3-3dxSRF3-OX* and the related
618 quantification [two-ways student test ($p<0.05$), n.s. non-significant]. Scale bar, 1cm. **(E)** Graph
619 showing time lapse of the root length of *srf3-3* under low iron (-Fe) medias in presence or absence
620 of DDG and the related quantification including the *srf3-2* mutant [ANOVA with post-hoc Tukey
621 test; Letters: statistical differences ($p<0.05$); Error bars: SEM].



623 **Figure 6. Coordination of bacterial immunity and iron homeostasis signaling pathways by**
624 **SRF3. (A)** Pictures of plants expressing *pCYP71A12::GUS* in WT and *srf3-4* under flg20 and
625 flg22 treatment (1μM, 24h) and the related quantification. Scale bars, 50μm. **(B)** Graph showing
626 time lapse of the root length of WT and *srf3-3* under flg20 and flg22 (1μM) [Error bars: SEM;
627 Asterix: significant difference between +Fe and -Fe for the WT according to a mixed effect model
628 ($p<0.05$)] and the related quantification including the *srf3-2* mutant [ANOVA with post-hoc Tukey
629 test; Letters: statistical differences ($p<0.05$)]. **(C)** Confocal images of 5 days old seedling
630 expressing *p35s::Lti6b-GFP* and *pUBQ10::SRF3-mCITRINE* in flg20 and flg22 (1μM, 4h) and the
631 related quantification [two-ways student test ($p<0.05$); n.s.: non-significant]. Scale bars, 10μm. **(D)**
632 Confocal images of 5 days old seedling stained with RhoNox-1 in WT in mock or flg22 (1μM, 1h)
633 and the related quantification [two-ways student test ($p<0.05$)]. Scale bars, 50μm. **(E)** Graph
634 representing the percentage of root showing *IRT1* promotor activation under mock and flg22
635 (1μM, 16h) treatment in WT and *srf3-4* in presence or absence of DDG. **(F)** Venn diagram of
636 differentially expressed genes under low iron levels (-Fe, 2h) and flg22 (1μM, 2h) in WT (left) in
637 *srf3* (middle) and DEGs in both condition between WT and *srf3*.
638
639
640
641
642
643
644
645
646
647
648
649
650
651
652
653
654
655
656
657
658
659
660
661
662
663
664
665
666
667
668
669
670
671

672 **Methods**
673

674 **Plant materials and growth conditions.** For surface sterilization, *Arabidopsis thaliana* seeds of
675 231 accessions from the Regmap panel (Spreadsheet S1) that had been produced under uniform
676 growth conditions were placed for 1 h in opened 1.5-mL Eppendorf tubes in a sealed box
677 containing chlorine gas generated from 130 mL of 10% sodium hypochlorite and 3.5 mL of 37%
678 hydrochloric acid. For stratification, seeds were imbibed in water and stratified in the dark at 4 °C
679 for 3 days. Seeds were then put on the surface of 1X MS agar plates, pH 5.7, containing 1%
680 (w/v) sucrose and 0.8% (w/v) agar (Duchefa Biochemie) using 12-cm x 12-cm square plates. The
681 iron-sufficient medium contained 100 µM Na-Fe-EDTA and the iron-deficient (1XMS iron free)
682 medium contained 300 µM Ferrozine, a strong iron chelator [3-(2-pyridyl)-5,6-diphenyl-1,2,4-
683 triazinesulfonate, Sigma Aldrich]¹¹. This condition was only used for GWAS. For further
684 experimentation, we used the Fe -sufficient or -free media described in Gruber et al., 2013, with
685 no or a decrease level of Ferrozine, 100, 50 and 10 µM. Using the Gruber et al., 2013 iron-free
686 medium, we add 300 µM of Na-Fe-EDTA to test *srf3* phenotype under iron excess⁵⁹. The *srf3-2*,
687 *srf3-3*, *bts-1*, *opt3-2*, *fls2-c*, *fls2-9*, *vit-1* and *cals3-3d* mutant lines are in Col-0 background and
688 were described and characterized^{16–18,34,60–62}. The reporter lines, *35s::PDBG1-mCITRINE*,
689 *35s::GFP-CALS3*, *pPDLP3::PDLP3-YFP*, *35s::GFP-PDLP5*, *35s::Lti6b-GFP*, *35s::DRONPA-s*,
690 *pSUC2::GFP* and *pCYP71A12::GUS* are in Col-0 background and were described and
691 characterized^{34,35,40,63–65}. The T-DNA insertion lines for SRF3, SAIL1176_B01 (*srf3-4*) and
692 SALK_202843, as well as for *at4g03400*, SAIL_811_C06 (*at4g03400*) were purchased from
693 Nottingham Arabidopsis Stock Center (NASC, Nottingham, United Kingdom). The primers used
694 for genotyping the T-DNA lines are listed below (List of primers, Spreadsheet S6). Plants were
695 grown in long day conditions (16/8h) in walk in growth chambers at 21°C, 50µM light intensity,
696 60% humidity. During nighttime, temperature was decreased to 15°C.

697
698 **Plant transformation and selection.** Each construct (see below: “Construction of plant
699 transformation vectors (destination vectors) and plant transformation”), was transformed into C58
700 GV3101 *Agrobacterium tumefaciens* strain and selected on YEB media (5g/L beef extract; 1g/L
701 yeast extract; 5g/L peptone; 5g/L sucrose; 15g/L bactoagar; pH 7.2) supplemented with antibiotics
702 (Spectinomycin, Gentamycin). After two days of growth at 28C, bacteria were collected using a
703 single-use cell scraper, re-suspended in about 200 mL of transformation buffer (10mM MgCl₂;
704 5% sucrose; 0.25% silwet) and plants were transformed by the floral dipping method⁶⁶. Plants
705 from the Columbia–0 (Col0) accession were used for transformation. Primary transformants (T1)
706 were selected *in vitro* on the appropriate antibiotic/herbicide (glufosinate for mCITRINE,
707 hygromycin for mCHERRY and mSCARLET tagged proteins). Approximately 20 independent T1s
708 were selected for each line. In the T2 generation at least 3 independent transgenic lines were
709 selected using the following criteria when possible: i) good expression level in the root for
710 detection by confocal microscopy, ii) uniform expression pattern, iii) single insertion line (1
711 sensitive to 3 resistant segregation ratio) and, iv) line with no obvious abnormal developmental
712 phenotypes. Lines were rescreened in T3 using similar criteria as in T2 with the exception that we
713 selected homozygous lines (100% resistant). At this step, we selected one transgenic line for
714 each marker that was used for further analyses and crosses.

715
716
717 **GWA mapping.** 231 natural accessions (12 plants/accession were planted) were grown on 1 ×
718 MS agar plates containing 300 µM Ferrozine under long day conditions (16 hours light) at 21°C.
719 Plant images were acquired by EPSON flatbed scanners (Perfection V600 Photo, Seiko Epson
720 CO., Nagano, Japan) every 24 hours for 5 days (2 DAG – 6 DAG). Root image analyses and trait
721 quantification were performed using the BRAT software⁶⁷. Median root growth rate (n ≥3) values
722 between 4 to 5 days were used for GWA study. For more accuracy, the roots not detected or not
723 germinated were not included in the analyses. GWA mapping was conducted using a mixed
724 model algorithm which has been used previously to correct population structure confounding and

725 SNP data from the 250K SNP chip⁶⁸⁻⁷². SNPs with minor allele counts equal or greater to 10 were
726 taken into account. The significance of SNP associations was determined at 5% FDR threshold
727 calculated by the Benjamini-Hochberg-Yekutieli method to correct for multiple testing⁷³. The
728 GWAS peak in proximity of *SRF3* (Figure 1a) contained 4 significant SNPs. By analyzing the
729 unique combinations of these 4 SNPs in the 231 accessions, four groups of haplotypes were
730 defined as Group A, Group B, Group C and Group D.
731

732 **Phenotyping of early root growth responses.** Seeds were sowed in +Fe media described in
733 Gruber et al., 2013 and stratified for 2-3 days at 4°C. Five days after planting, about 15 seedlings
734 were transferred to a culture chamber (Lab-Tek, Chamberes #1.0 Borosilicate Coverglass
735 System, catalog number: 155361) filled with – Fe or +Fe medium described in Gruber et al., 2013
736 or +Fe medium containing flg20 or flg22. Note that the transfer took about 45-60 seconds. Images
737 were acquired every 5 minutes for 12 hours representing 145 images per root in brightfield
738 conditions using a Keyence microscope model BZ-X810 with a BZ NIKON Objective Lens (2X)
739 CFI Plan-Apo Lambda.
740

741 **Phenotyping of late root growth responses.** Seeds were sowed in +Fe media described in
742 Gruber et al., 2013 and stratified for 2-3 days at 4°C. Five days after planting, 6 plants per
743 genotype were transferred to four 12x12cm plates in a pattern in which the positions of the
744 genotypes were alternating in a block design (top left, top right, bottom left and bottom right). After
745 transfer, the plates were scanned every 24 hours for 3 days using the BRAT software⁶⁷.
746

747 **Quantitative real time PCR.** For *SRF3* expression analysis seedlings were grown initially on iron
748 sufficient media (1xMS, 1% w/v Caisson Agar) for 5 days and then shifted to either iron sufficient
749 or low iron (100 uM FerroZine) 1xMS liquid medium. Nylon mesh (Nitex Cat 03-100/44; Sefar)
750 was placed on top of the solidified media to facilitate transfer. Root tissues were collected for RNA
751 extraction 3 hours post transfer by excision with fine scissors. Each biological replicate was
752 constituted by RNA extraction from 30-40 whole roots. Samples were immediately frozen in liquid
753 nitrogen, ground, and total RNA was extracted using the RNeasy Plant Mini kit (QIAGEN GmbH,
754 Hilden, Germany). qRT-PCR reactions were prepared using 2x SensiMix SYBR & Fluorescein Kit
755 (PEQLAB LLC, Wilmington, DE, USA) and PCR was conducted with a Roche Lightcycler 96
756 (Roche) instrument. Relative quantifications were performed for all genes with the β -tubulin gene
757 (AT5G62690) used as an internal reference. The primers used for qRT-PCR are shown in list of
758 primers (Spreadsheet S6).
759

760 **RNAseq.** Total RNA was extracted from roots of plants 5 days after germination using RNA
761 protein purification kit (Macherey-Nagel). Next generation sequencing (NGS) libraries were
762 generated using the TruSeq Stranded mRNA library prep kits (Illumina, San Diego, CA, USA).
763 Libraries were sequenced on a HiSeq2500 (Illumina, San Diego, CA, USA) instrument as single
764 read 50bases. NGS analysis was performed using Tophat2 for mapping reads onto the
765 Arabidopsis genome (TAIR10)⁷⁴, HT-seq for counting reads and EdgeR for quantifying differential
766 expression⁷⁶. We set a threshold for differentially expressed genes (Fold change (FC) >2 or FC<-
767 2, FDR<0.01). Genotype x Environment interaction analysis was performed using linear model
768 and type II Anova analyses in R (codes are available upon request). Gene ontology analysis was
769 performed using the AgriGOv2 online tool⁷⁷. Venn diagrams were generated with the VIB online
770 tool (<http://bioinformatics.psb.ugent.be/webtools/Venn/>). The plot in figure 3a was generated
771 using the online Revigo software (<http://revigo.irb.hr/>).
772
773

774 **Microscopy setup.** All imaging experiments except when indicated below, were performed with
775 the following spinning disk confocal microscope set up: inverted Zeiss microscope equipped with
776 a spinning disk module (CSU-X1, Yokogawa, <https://www.yokogawa.com>) and the prime 95B
777 Scientific CMOS camera (<https://www.photometrics.com>) using a 63x Plan- Achromat objective
778 (numerical aperture 1.4, oil immersion) or low resolution 10x lens for time lapse imaging. GFP,
779 mCITRINE, Aniline blue and RhoNox-1 staining were excited with a 488 nm laser (150mW) and
780 fluorescence emission was filtered by a 525/50 nm BrightLine® single-band bandpass filter.
781 mSCARLET, mCHERRY and propidium iodide dyes were excited with a 561 nm laser (80 mW)
782 and fluorescence emission was filtered by a 609/54 nm BrightLine® single-band bandpass filter
783 (Semrock, <http://www.semrock.com/>). 405 nm laser was used to excite aniline blue and emission
784 was recorded at 480–520 nm with 40x objectives. For propidium iodide, 488nm for excitation and
785 around 600nm was used with 40x objectives. For quantitative imaging, pictures of root cells were
786 taken with detector settings optimized for low background and no pixel saturation. Care was taken
787 to use similar confocal settings when comparing fluorescence intensity or for quantification.

788 **FRAP experiment.** Fluorescence in a rectangle ROI (50 μm^2 , 15 μm long), in the plasma
789 membrane region, was bleached in the root optical section by four successive scans at full laser
790 power (150 W) using the FRAP module available on the Zeiss LSM 980 Airyscan 2. Fluorescence
791 recovery was subsequently analysed in the bleached ROIs and in controlled ROIs (rectangle with
792 the same dimension in unbleached area). FRAP was recorded continuously during 90 s with a
793 delay of 0.3 s between frames. Fluorescence intensity data were normalized as previously
794 described (Platre et al, 2019). For visualization, kymographs were obtained using kymograph
795 function in Fiji.

796 **TIRF microscopy.** Total Internal Reflection Fluorescence (TIRF) Microscopy was done using the
797 inverted ONI Nanoimager from Oxford microscope with 100x Plan-Apochromat objective
798 (numerical aperture 1.50, oil immersion). The optimum critical angle was determined as giving the
799 best signal-to-noise ratio. Images were acquired with about 15% excitation (1W laser power) and
800 taking images every 100ms for 500-time steps.

801 **DRONPA-s bleaching and activation.** 5 day-old seedlings were transferred to a culture chamber
802 (Lab-Tek, Chamberes #1.0 Borosilicate Coverglass System, catalog number: 155361) filled with
803 – Fe or +Fe medium described in Gruber et al., 2013⁵⁹ for 4 hours. After 4 hours, the cell wall was
804 counter-stained by placing one drop of propidium iodide 15 μM (10 $\mu\text{g}/\text{mL}$ in distilled water) on
805 the root tip for 1 minutes. A coverslip was placed on the surface of the root for further imaging.
806 DRONPA-s was bleached using the full laser power (150 W) of the 488nm laser for 10 seconds.
807 Then 2-4 regions of interest (ROIs) were drawn on the external lateral side of the epidermal root
808 cells and DRONPA-s was activated in this region using the 405 nm laser doing 8 cycles at 15W
809 using the FRAP module available on the Zeiss LSM 980 Airyscan 2. Right after activation and
810 then again 6 minutes later, images were acquired in both channel, PI and DRONPA-s.

811 **IRT1 reporter lines after 24h.** About 24 of 5-day-old seedlings grown on iron sufficient medium
812 were transferred to agar plate filled with +Fe or – Fe supplemented with 100 Ferrozine for 24
813 hours. 15 seedlings were transferred to a culture chamber (Lab-Tek, Chamberes #1.0 Borosilicate
814 Coverglass System, catalog number: 155361) filled with +Fe described in Gruber et al., 2013⁵⁹.
815 The cell wall was counter-stained by placing one drop of propidium iodide 15 μM (10 $\mu\text{g}/\text{mL}$ in
816 distilled water) on the root tip for 1 minutes. A coverslip was placed on the surface of the root for
817 further imaging. Images were acquired using the spinning disc set up described above using
818 stitching and z-stack modes.
819

820 **Time lapse imaging of IRT1 reporter lines.** 5-day-old seedlings were grown on iron sufficient
821 medium and then about 15 seedlings were transferred to a culture chamber (Lab-Tek, Chamberes
822 #1.0 Borosilicate Coverglass System, catalog number: 155361) filled with +Fe or – Fe medium
823 described in Gruber et al., 2013⁵⁹ or +Fe medium containing flg22. Note that the transfer took
824 about 45-60 seconds. Images were acquired every 20 minutes for 16 hours representing 80
825 images per root using a Keyence microscope model BZ-X810 with BZ NIKON Objective Lens
826 (2X) CFI Plan-Apo Lambda in brightfield, green (ET470/40x ET525/50m T495lpxr-UF1) or red
827 (ET560/40x ET630/75m T585lpxr-UF1) channels.
828

829 **Time lapse imaging of SRF3 transcriptional and translational reporter and control lines**
830 About 15 5-day-old seedlings grown on iron sufficient medium were transferred to a culture
831 chamber (Lab-Tek, Chamberes #1.0 Borosilicate Coverglass System, catalog number: 155361)
832 filled with +Fe or – Fe medium described in Gruber et al., 2013. Note that the transfer took about
833 45-60 seconds. Images were acquired every 10 minutes for 4 hours using the spinning disc set
834 up described above and assembled using the stitching mode, z-satck and definite focus options
835 to keep track of the root and be localized at the same z-stage a long time, respectively.
836

837
838 **Cryofixation and freeze-substitution.** 5-day-old seedlings of pSRF3::SRF3-GFP line
839 (*Landsberg erecta* background) and LER were grown vertically on Caisson media complemented
840 in iron. The seedlings were incubated for 4 hours in liquid Caisson media which were
841 complemented or deficient in iron. Root tips were taken and cryofixed in 20% BSA filled copper
842 platelets (100 nm deep and 1.5 mm wide) with EM PACT1 high pressure freezer (Leica). The
843 samples were transferred for freeze-substitution in AFS2 (Leica) at -90°C in cryosubstitution mix:
844 uranyl acetate 0.36%, in pure acetone, for 24 hours. The temperature was raised stepwise by 3°C
845 h⁻¹ until reaching -50°C and maintained for 3 hours. The cryosubstitution mix was removed and
846 replaced by pure acetone and then pure ethanol, for each of them 3 washes of 10 minutes were
847 performed. The copper platelets were not removed in order to avoid sample loss. HM20 Lowicryl
848 resin (Electron Microscopy Science) solutions of increasing concentrations were used for
849 infiltration: 25% and 50% (1 hour each), 75% (2 hours), 100% (overnight, 4 hours, 48 hours- each
850 bath was performed with new resin). The samples were then polymerized under ultraviolet light
851 for 24 hours at -50°C before raising the temperature stepwise by 3°C h⁻¹ until reaching 20°C and
852 maintained for 6 hours.
853

854 **Immunogold labelling.**
855 The samples were recovered by removing exceeding resin on the top and edges of the copper
856 platelets. The latter were removed by applying alternatively heat shocks with liquid nitrogen and
857 on a 40°C heated knife to dissociate copper platelet from the resin. Ultrathin sections of 90 nm
858 thickness were trimmed at a speed of 1 mm s⁻¹ (EM UC7 ultramicrotome, Leica) and recovered
859 on electron microscopy grids (T 300mesh copper grids, Electron Microscopy Science) covered
860 by 2% parlodion film. Once the grids were dry immunogold labelling was performed. The grids
861 were successively incubated in 10 µl droplets of different reagents (0.22 µm filtered). The grids
862 were first incubated in PHEM Tween 0.2% BSA 1% buffer (pH6.9) for 1 minute of rinsing before
863 30 minutes of blocking. The primary antibody anti-GFP rabbit polyclonal antibody (A11122,
864 Thermo Fisher Scientific) and secondary antibody 10 nm colloidal gold-conjugated goat anti-rabbit
865 IgG (Tebu-Bio) were diluted in PHEM Tween 0.2% BSA 1% buffer (pH6.9) to 1/200 and 1/40

866 respectively and grids were incubated for 1 hour. 3 rinsing steps of 5 minutes each were
867 performed between the primary and secondary antibody incubation and after the secondary
868 incubation. The grids were rinsed on filtered milliQ water droplets before drying and imaging.
869 Image acquisition was performed at 42000x magnification on a FEI Tecnai G2 Spirit TWIN TEM
870 with axial Eagle 4K camera.

871

872 **Immunolocalization of callose.**

873 Arabidopsis seedlings were grown on ½ MS 1% sucrose agar plate for 6 days and then incubated
874 for 3 hours in ½ MS 1% sucrose liquid medium for control condition or ½ MS 1% sucrose liquid
875 medium containing 0.4 M mannitol, prior to fixation. The immunolocalization procedure was done
876 according to Boutté *et al.* 2014⁷⁸. The callose antibody (Australia Biosupplies) was diluted to
877 1/300 in MTSB (Microtubule Stabilizing Buffer) containing 5% of neutral donkey serum. The
878 secondary anti-mouse antibody coupled to TRITC (tetramethylrhodamine) was diluted to 1/300 in
879 MTSB buffer containing 5% of neutral donkey serum. The nuclei were stained using DAPI (4',6-
880 diamidino-2-phénylindole) diluted to 1/200 in MTSB buffer for 20 minutes. Samples were then
881 imaged with a Zeiss LSM 880 using X40 oil lens. DAPI excitation was performed using 0,5% of
882 405 laser power and fluorescence collected at 420-480 nm; GFP excitation was performed using
883 5% of 488 nm laser power and fluorescence emission collected at 505-550 nm; TRITC excitation
884 was performed with 5% of 561 nm power and fluorescence collected at 569-590 nm. All the
885 parameters were kept the same between experiments to allow quantifications.

886

887 **Short-term iron deficiency, flg20 and flg22 treatments.** Seeds were sowed in +Fe medium
888 described in Gruber *et al.*, 2013 and stratified for 2-3 days at 4°C. 5-day-old seedlings were
889 treated for 4 hours with low iron medium or for 2 hours adding 100uM of FerroZine or sufficiency
890 in liquid medium described in Gruber *et al.*, 2013 using 12-well plates. Note that after the addition
891 of FerroZine the pH was adjusted to the same pH=5.7 as the control medium +Fe. However, no
892 change in the pH was detected in agar adjusted with MES as described earlier and in Gruber *et*
893 *al.*, 2013. For flg22 treatment, Seeds were sowed in +Fe medium described in Gruber *et al.*, 2013
894 and stratified for 2-3 days at 4°C. 5-day-old seedlings were treated for 4 hours in iron sufficient
895 media described in Gruber *et al.*, 2013 supplemented or not with flg22 or flg20.

896

897 **RhoNox-1 staining.** 5-day-old seedlings were treated in ultra-pure distilled water (Fisher
898 Scientific Invitrogen UltraPure Distilled Water 500 mL Plastic Container – 10977015) called +Fe
899 condition in order to get rid of any iron trace in water, 50uM of FerroZine was added for 30 minutes.
900 Then, the plants were transferred to ultra-pure distilled water supplemented with 2.5uM of
901 RhoNox-1 for 15 minutes (stock solution 5mM; <https://goryochemical.com/>).

902

903 **Perls staining and DAB/H₂O₂ intensification.** Perls staining and DAB/H₂O₂ intensification was
904 performed as described previously (Roschztardt *et al.*, 2009). The embryos were dissected and
905 isolated from dry seeds previously imbibed in distilled water for 3-4 h. The embryos were then
906 vacuum infiltrated with Perls stain solution (equal volumes of 4% (v/v) HCl and 4% (w/v) K-
907 ferrocyanide) for 15 min and incubated for 30 min at room temperature (Stacey *et al.*, 2008). The
908 DAB intensification was performed as described in Meguro *et al.*, 2007. After washing with
909 distilled water, the embryos were incubated in a methanol solution containing 0.01 M NaN₃ and
910 0.3% (v/v) H₂O₂ for 1 h, and then washed with 0.1 m phosphate buffer (pH 7.4). For the
911 intensification reaction the embryos were incubated between 10 to 30 min in a 0.1 M phosphate
912 buffer (pH 7.4) solution containing 0.025% (w/v) DAB (Sigma), 0.005% (v/v) H₂O₂, and 0.005%
913 (w/v) CoCl₂ (intensification solution). The reaction was terminated by rinsing with distilled water.

914

915 **GUS Histochemical Assay**

916 Transgenic seedlings carrying *pCYP71A12:GUS* were grown on ½ MS media for 4 days and
917 seedlings were then grown in 6 well plates containing ½ MS (+Fe or -Fe) liquid media for 16
918 hours. Seedlings were then treated with 1 µM Flg22 or 1 µM Flg20 for 16 hours. After treatment
919 with peptides plants were washed with 50 mM sodium phosphate buffer, pH 7. One milliliter of
920 GUS substrate solution (50 mM sodium phosphate, pH 7, 10 mM EDTA, 0.5 mM K₄[Fe(CN)₆],
921 0.5 mM K₃[Fe(CN)₆], 0.5 mM X-Gluc, and 0.01% Silwet L-77) was poured in each well. The plants
922 were vacuum infiltrated for 5 min and then incubated at 37°C for 4 h. Tissues were observed
923 using a Discovery V8 microscope (Zeiss). Quantification of GUS signal in root tips of the stained
924 seedlings was done using Fiji.

925
926

927 **Aniline blue staining.** 5 day-old seedlings were incubated for 2h in iron deficient or sufficient
928 medium⁵⁹ with or without DDG and then transferred for 2 hours to 150 mM K₂HPO₄ and 0.01%
929 aniline blue in 12-well plates wrapped in aluminum foil for light protection. Then imaging of the
930 root epidermis in the elongation zone was performed.

931

932 **Sterol treatments.** For inhibitor experiments, 5-day-old seedlings were transferred to MS agar
933 plates containing 50 µg/mL Fenpropimorph (<https://www.caymanchem.com/>;
934 50 µg/µL in DMSO) or 1 µM Lovastatin (https://www.tocris.com/products/lovastatin_1530;
935 1 mM in DMSO) for 24 hours.

936

937 **2-deoxy-d-glucose (DDG) treatment.** Seedlings were grown on iron sufficient medium and after
938 5 days transferred to iron sufficient or low iron medium or flg22 containing medium with or without
939 DDG (diluted in H₂O, stock 50mM used at 50µM; [https://www.tocris.com/products/2-deoxy-d-](https://www.tocris.com/products/2-deoxy-d-glucose_4515)
940 [glucose_4515](https://www.tocris.com/products/2-deoxy-d-glucose_4515)).

941

942

943

944

945

946

947

948 QUANTIFICATION

949 **Late root growth response.** Plates containing seedlings were scanned from days 5 to 9 after
950 transfer to different media in order to acquire images for further quantification of the root growth
951 rate per conditions. Plates were scanned using BRAT software⁶⁷ each day and were stacked
952 together using a macro in Fiji (Macro_Match_Align). We then calculated the root length for every
953 day per genotype in each condition to evaluate the root growth rate in Fiji using the segmented
954 line. We first calculated the mean of the root growth rate for each days 5 to 6, 6 to 7, 7 to 8, 8 to
955 9. These values were used to calculate the mean of root growth rate for 3 days . Then, we divided
956 the mean of root growth rate for 3 days to a given media for each plant by the mean of root growth
957 rate for 3 days after transfer to the control media for the entire related genotype. This ratio was
958 used as the late root growth response to low iron levels Every experiment was repeated twice.

959

960 **Early root growth response.** Root length for each seedling was recorded for 12 hours taking a
961 picture every 5 minutes and quantified using a Matlab script (Matlab_RootWalker). From these

962 measurements, we plotted the root length from T0 to T12 after transfer. We obtain a curve
963 representing the root length after transfer from which we calculated the area under the curve using
964 the following formula “(Root length T1+Root length T2)/2*(Time T2-Time T1)”. Then, we divided
965 the value of the area under the curve after transfer for each plant in a given condition by the area
966 under the curve after transfer to the control media for the entire related genotype. This ratio was
967 used as the early root growth response to low iron levels. Every experiment has been repeated
968 three times.

969
970 **Lateral root density.** 12-day-old seedlings were used for quantification for the lateral root assays.
971 Plates were scanned using BRAT software⁶⁷. A ratio of the number of lateral roots divided by the
972 root length was applied in order to calculate the lateral root density. This final value was used for
973 further analysis. This experiment has been repeated twice.

974
975 **Root meristem size.** 5 days old seedlings were transferred to iron sufficient or deficient medium
976 (as described in Gruber et al., 2013) that was contained in small chambers used for the early root
977 growth response (Lab-Tek, Chamberes #1.0 Borosilicate Coverglass System, catalog number:
978 155361). After 12 hours, the cell wall was stained by placing one drop of propidium iodide 15 μM
979 (10 $\mu\text{g}/\text{mL}$ in distilled water) on the root tip for 5 minutes. Images were acquired using the stitching
980 mode on the microscope. The cell size was determined using the Cell-O-Type software in the
981 cortex cells⁷⁹. Every experiment has been repeated three times.

982
983 **Measuring signal intensities at the plasma membrane.** Confocal images were first denoised
984 using an auto local threshold applying the Otsu method with a radius of 25 and a median filter
985 with a radius of 2 in Fiji⁸⁰. In order to remove every single bright pixel on the generated-binary
986 image the despeckle function was applied. In order to obtain plasma membrane skeleton, we
987 detected and removed every intracellular dot using the “Analyze Particles” plugin with the
988 following parameter, size between 0.0001 and 35 000 μm^2 and a circularity between 0.18 and 1.
989 Then, we selected and cropped a zone which only showed a proper plasma membrane skeleton.
990 We created a selection from the generated-plasma membrane skeleton and transposed it to the
991 original image to calculate the plasma membrane intensity. This process has been automatized
992 in a Macro (Macro_PM_Intensity). The plasma membrane intensity value was then divided by the
993 total intensity of the image to normalize the plasma membrane intensity. An average of 45 cells
994 were used for quantification per root. Every experiment was repeated three times.

995
996 **Calculating standard deviation measures of the intensities at the plasma membrane.** The
997 standard deviation of the apical-basal plasma membrane was calculated using the segmented
998 lines in Fiji toolbox with a width of 3 pixels. 5 plasma membranes were used per root and the
999 mean was calculated per root. Every experiment has been repeated three times.

1000
1001 **Fluorescence intensity in the root tip during time lapse experiments.** To acquire images, z-
1002 stacks with a stepsize of 50 μm were performed coupled with the stitching mode. To determine
1003 the variation of our translational and transcriptional reporters under different condition, we
1004 measured the signal intensity in the root tip over time using Fiji. Prior analysis, confocal images
1005 were stitched, and we generate the maximum intensity projection. We drew a region of interest of
1006 the same size in the x and y dimensions, corresponding to the width of the root and in length
1007 corresponding to the basal meristem, transition and elongation zones. In this region, for each time
1008 point we determined the mean grey value. Note that this value is normalized since for each root
1009 the same area has been kept between conditions and genotypes. Every experiment was repeated
1010 three times.

1011

1012 **Polarity Index.** 5 days old seedlings of transgenic lines were analyzed to determine the “Polarity
1013 index” in root tip epidermis. “Polarity index” is the ratio between the fluorescence intensity (Mean
1014 Grey Value function of Fiji software) measured at the PM apical/basal side and PM lateral sides
1015 (Line width=3). We selected only cells for which the PM at each pole (apical, basal and laterals)
1016 were easily viewable and we selected cells that were entering elongation (at least as long as wide,
1017 but no more than twice as long as wide). Quantification was conducted in 100 cells over more
1018 than 15 independent plants. This Polarity index reveals the degree of polarity of the fluorescent
1019 reporters between the apical/basal side and lateral sides of the PM. Every experiment was
1020 repeated three times

1021
1022 **Integrated Nuclear and fluorescence signal density of transcriptional reporter lines.** To
1023 acquire images, z-stacks with a stepsize of 50 μm were performed coupled with the stitching
1024 mode. Then, we generated the maximum intensity projection for the z-dimension and then
1025 binarized the images using the auto local threshold Bernsen with a radius of 15. The despeckle
1026 and erode functions were subsequently used to remove background artefacts. The nucleus in this
1027 region were selected using the analyze particles function with the settings for size of 15 and 700
1028 μm^2 and for circularity 0.25 to 1.00. The regions selected were used on the original picture for
1029 determining the fluorescence intensity in each nucleus. Then the average nuclear integrated
1030 density was calculated per root in order to normalize the intensity by the total root area. This
1031 process has been automatized in a macro in Fiji (Macro_Nuclear_Signal_Intensity). From the
1032 same images, the number of nuclei was calculated and the root area was detected using the
1033 plugin “Wavelet a trou” (<http://www.ens-lyon.fr/RDP/SiCE/METHODS.html>)⁸¹. The number of
1034 nuclei detected was then divided by the area of the respective root to determine the nuclear
1035 density per root. This process was automatized using a Fiji macro (Macro_Nuclear_Density).
1036 Every experiment was repeated three times.

1037
1038 **IRT1 promotor activation in time lapse serie.** At each time point, roots showing fluorescence
1039 signal in the apical 3 mm of the root were counted. Roots that were already showing activation in
1040 this zone or showed slight signals at timepoint 0 were removed from the analysis. Then the
1041 number of roots that started to show a fluorescent signal after timepoint 0, was divided by the
1042 number of total roots observed in this experiment and multiplied by 100 to obtain the percentage
1043 of root showing pIRT1 activation in the apical 3 mm of the root. Every experiment was repeated
1044 three times.

1045 **Distance of signals from the Quiescent Center in the SRF3 transcriptional reporter line.**
1046 Based on the propidium iodide staining, the Quiescent Center (QC) region was determined by its
1047 morphology. Then, using the straight-line option in Fiji, a line was traced from the QC to the first
1048 appearance of a clear, bright signal that reported pSRF3 activity. The distance along this line was
1049 calculated to determine the distance from the QC to the first cell expressing *pSRF3* in the
1050 elongation zone. Every experiment was repeated three times.

1051 **DRONPA-s diffusion.** After activation of the DRONPA-s reporter, the signal intensity using the
1052 integrated density of the signal was calculated in the activated cells as well as the adjacent upper
1053 and lower cells using Fiji. The signal intensity once again was calculated in the same regions 6
1054 minutes after the activation. To account for photo bleaching, these values were normalized by
1055 dividing the DRONPA-s signal intensity after and post bleach in a zone where DRONPA-s was
1056 visible in both images. The average of the normalized integrated density in the surrounding cells
1057 was calculated, averaging the values obtained in upper and lower cells. Finally, the ratio of the
1058 normalized integrated density after and post bleach was calculated by dividing both values to
1059 obtain the DRONPA-s normalized fluorescence intensity. Every experiment was repeated three
1060 times.

1061
1062 **pSUC2::GFP diffusion.** In order to evaluate the diffusion of the GFP protein, a ROI of about 1800
1063 μm^2 was drawn at the root tip of each root using Fiji. The mean gray value was calculated and
1064 divided by the corresponding area to normalize the value. Every experiment was repeated three
1065 times.

1066
1067 **RhoNOx-1 signal intensity.** The root area was detected using the plugin “Wavelet a trou”
1068 (<http://www.ens-lyon.fr/RDP/SiCE/METHODS.html>)⁸¹ and then in this area the mean gray value
1069 was calculated and divided by the size of the size of the area to obtain the normalized signal
1070 intensity. This process has been automatized on a Fiji Macro, Macro_RhoNox-1

1071
1072 **Aniline blue fluorescence intensity.** Using Fiji, the mean gray value of 10 plasma membranes
1073 in the apical-basal side of the epidermis in the transition-elongation zone was calculated with the
1074 segmented line option with 3 pixels wide. The mean of these values was then divided by the mean
1075 gray value in the total area where the plasma membrane signal has been calculated in order to
1076 normalize the value due to differential strength of the staining. This final value was used for further
1077 analysis. Every experiment was repeated three times.

1078
1079
1080 **Anti-callose antibody fluorescence intensity**
1081 Callose deposition was quantified using the Fiji software. Callose fluorescence intensity was
1082 measured at the apico-basal cell walls of root epidermal and cortex cells using the segmented
1083 line with a width of 3 pixels. A total of 8 to 10 cell walls were measured per roots and used to
1084 calculate the average of anti-callose fluorescence intensity per root. Between 5 to 20 roots per
1085 transgenic lines and conditions were used in two independent biological replicates were used.

1086
1087 **Immunogold**
1088 The number of gold particles in the EM micrographs were quantified using Fiji software. The
1089 number of particles were counted manually in each compartment; e.g. Cytosol, Cell wall, PM and
1090 PD; and then reported relative to the surface of cytosol or cell wall ($/\mu\text{m}^2$), to the length of PM
1091 ($/\mu\text{m}$) and to individual PD. A total of 25 to 50 micrographs were analyzed for each line and
1092 conditions. Two biological replicates were used.

1093 **STATISTICS**

1094
1095 Each experiment has been repeated independently at least twice, as in every cases the same
1096 trend has been recorded for independent experiment, the data the different has been pooled for
1097 further statistical analysis. Each sample were subjected to four different normality tests (Jarque-
1098 Bera, Lilliefors, Anderson-Darling and Shapiro-Wilk), sample were considered as a Gaussian
1099 distribution when at least one test was significant ($p=0.05$) using Xlstat.

1100
1101 - As a normal distribution was observed a one-way ANOVA coupled with post hoc Tukey
1102 honestly significant difference (HSD) test was performed ($p=0.05$) using R software or
1103 Xlstat. Figures: 1F, 2A, 3A, 4A, 4B, 4C, 4D, 5E, 6B, S2C, S2D, S2F, S3C, S4A, S4B, S8C,
1104 S9D, S11A, S11B, S12B, S12C, S12D, S12E, S13D, S13E, S17C, S17D.

1105
1106 - As a normal distribution was observed at one-way ANOVA coupled with post hoc Lowest
1107 significant difference (LSD) test was performed ($p=0.05$) using Xlstat: 5E.

1108
1109 - As a normal distribution was observed an independent two-ways student test was
1110 performed ($p=0.05$) using Xlstat. Figures: 1C, 1D, 2D, 5D, 6C, 6D, S2E, S4C, S7B (left
1111 panel), S7C, S10A, S10B, S10C, S11C, S14A, S14C (both panel).

- 1112
1113 - As a normal distribution was not observed at two-ways Kruskal-Wallis coupled with post
1114 hoc Steel-Dwass-Critchlow-Fligner procedure was performed ($p=0.05$) using Xlstat.
1115 Figure: S9C.
1116
1117 - As a normal distribution was not observed a two-ways Mann-Whitney test was performed
1118 ($p=0.05$) using Xlstat. Figures: S7B (right panel)
1119

1120 For time lapse analysis SAS software was used based on a mixed effect model ($p<0.05$) to test
1121 the statistical significance. Figures: 2C
1122

1123 CLONING

1124 **pIRT1 transcriptional reporter line:**

1126 To generate the transcriptional pIRT1::NLS-2xYPet reporter line, the *IRT1* promoter (2.6 kb) was
1127 cloned at *SalI* and *BamHI* restriction sites using the primers pIRT1 Sal_F and pIRT1 Bam_R in
1128 the pBJ36 vector carrying two in frame copies of the YPet yellow fluorescent protein fused to
1129 SV40 nuclear localization signal (kind gift of Dr. Jeff D.B. Long, UCLA). The *pIRT1::2xYPet-NLS*
1130 cassette was digested with *NotI* and cloned in the pART27 binary vector⁸². Note that About 20
1131 independent T1 lines were isolated and between three to six representative mono-insertion lines
1132 showing strong activation of *IRT1* promoter in the root epidermis upon low iron, as previously
1133 described (Vert et al., 2002), were selected in T2.
1134

1135 **SRF3 constructs in Ler**

1137 To generate pSRF3::SRF3g-GFP from *Ler* background, the SRF3 gene and its native promoter
1138 (-1492 nt from the transcription start) was amplified by PCR using genomic DNA as template and
1139 the primers attB1-SRF3Ler_F and attB2-SRF3Ler_R. The resulting amplicon was purified,
1140 sequenced and subcloned into pDONR221 by Gateway BP recombination, following
1141 manufacturer's instructions. To generate the C-terminus GFP fusion, the pSRF3::SRF3g fragment
1142 was cloned into the binary vector pGWB450 (Nakagawa et al., 2007) by Gateway LR
1143 recombination.
1144

1145 **SRF3 constructs (entry vectors):**

1146 The full-length coding sequence of SRF3 (At4g03390) was amplified by RT-PCR using 7-day old
1147 Arabidopsis seedlings cDNA as template and the SRF3_CDS_p221_F and
1148 PSRF3_CDS_p221_noSTOP_R primers. The corresponding PCR product was recombined into
1149 pDONR221 vector by BP reaction to give SRF3cds-noSTOP/pDONR221. To remove the SRF3
1150 extracellular domain the primers SRF3_kinase_p221_F and SRF3_kinase_p221_R. The
1151 corresponding PCR product was recombined into pDONR221 vector by BP reaction to give
1152 SRF3cds Δ extraC_p221.

1153 To remove the SRF3 kinase domain 5' phosphorylated primers were used SRF3_ Δ Kinase2-5'_F
1154 and SRF3_ Δ Kinase-5'_R followed by a ligation to give SRF3cds Δ Kinase_pDONR221.

1155 SRF3 mutant impaired in the kinase activity was obtained by site directed mutagenesis using
1156 SRF3-cds_mutKD_p221_F and SRF3-cds_mutKD_p221_R to give SRF3cds
1157 KDmut_pDONR221.
1158

1159 **Promoters and fluorescent proteins (entry vectors):**

1161 The *SRF3* promoter (5078bp upstream of 5'UTR until the 3'UTR of the previous gene) was cloned
1162 using the gibbon cloning method (<https://www.neb.com/applications/cloning-and-synthetic->

1163 biology/dna-assembly-and-cloning/gibson-assembly#tabselect3) with the following primers,
1164 Insert_pSRF3_F, Insert_pSRF3_R and Backbone_pSRF3_F and Backbone_pSRF3_R
1165 introduced into the P4P1R vector (life technologies www.lifetechnologies.com/) to give
1166 SRF3prom/pDONR4P1R.

1167
1168 The fluorescent mSCARLET protein was synthesized (GeneArt, www.thermofischer.com),
1169 amplified with attB2r and attB3 gateway sites using the mSCARLET_F and
1170 mSCARLETwSTOP_R primers, and then recombined into pDONRP2R-P3 by BP reaction to yield
1171 the mSCARLET/pDONRP2R-P3 entry vector.

1172
1173
1174
1175
1176
1177
1178
1179
1180
1181
1182
1183
1184
1185
1186
1187
1188
1189
1190

1191 **References:**

- 1192
- 1193 1. Kramer, J., Özkaya, Ö. & Kümmerli, R. Bacterial siderophores in community and host
1194 interactions. *Nature Reviews Microbiology* **18**, 152–163 (2020).
 - 1195 2. Kobayashi, T. & Nishizawa, N. K. Iron Uptake, Translocation, and Regulation in Higher
1196 Plants. *Annual Review of Plant Biology* **63**, 131–152 (2012).
 - 1197 3. Cassat, J. E. & Skaar, E. P. Iron in Infection and Immunity. *Cell Host & Microbe* **13**, 509–
1198 519 (2013).
 - 1199 4. Ganz, T. & Nemeth, E. Iron homeostasis in host defence and inflammation. *Nat Rev*
1200 *Immunol* **15**, 500–510 (2015).

- 1201 5. Iatsenko, I., Marra, A., Boquete, J.-P., Peña, J. & Lemaitre, B. Iron sequestration by
1202 transferrin 1 mediates nutritional immunity in *Drosophila melanogaster*. *PNAS* **117**, 7317–
1203 7325 (2020).
- 1204 6. Bai, L. *et al.* Phylogenomic analysis of transferrin family from animals and plants. *Comp*
1205 *Biochem Physiol Part D Genomics Proteomics* **17**, 1–8 (2016).
- 1206 7. Verbon, E. H., Trapet, P. L., Stringlis, I. A. & Kruijs, S. Iron and Immunity. *Annual Review*
1207 *of Phytopathology* **55**, 1–15 (2017).
- 1208 8. Deák, M. *et al.* Plants ectopically expressing the iron-binding protein, ferritin, are tolerant to
1209 oxidative damage and pathogens. *Nat. Biotechnol.* **17**, 192–196 (1999).
- 1210 9. Segond, D. *et al.* NRAMP genes function in *Arabidopsis thaliana* resistance to *Erwinia*
1211 *chrysanthemi* infection. *The Plant Journal* **58**, 195–207 (2009).
- 1212 10. Aznar, A. *et al.* Scavenging Iron: A Novel Mechanism of Plant Immunity Activation by
1213 Microbial Siderophores1[C][W]. *Plant Physiol* **164**, 2167–2183 (2014).
- 1214 11. Dinnyen, J. R. *et al.* Cell identity mediates the response of *Arabidopsis* roots to abiotic stress.
1215 *Science* **320**, 942–945 (2008).
- 1216 12. Zamioudis, C. *et al.* Rhizobacterial volatiles and photosynthesis-related signals coordinate
1217 MYB72 expression in *Arabidopsis* roots during onset of induced systemic resistance and
1218 iron-deficiency responses. *Plant J.* **84**, 309–322 (2015).
- 1219 13. Palmer, C. M., Hindt, M. N., Schmidt, H., Clemens, S. & Guerinot, M. L. MYB10 and
1220 MYB72 Are Required for Growth under Iron-Limiting Conditions. *PLOS Genetics* **9**,
1221 e1003953 (2013).
- 1222 14. Xing, Y. *et al.* Bacterial effector targeting of a plant iron sensor facilitates iron acquisition
1223 and pathogen. *The Plant Cell Online* 31 (2021).

- 1224 15. Hirayama, T. Development of Chemical Tools for Imaging of Fe(II) Ions in Living Cells: A
1225 Review. *Acta Histochem Cytochem* **51**, 137–143 (2018).
- 1226 16. Mendoza-Cózatl, D. G. *et al.* OPT3 Is a Component of the Iron-Signaling Network between
1227 Leaves and Roots and Misregulation of OPT3 Leads to an Over-Accumulation of Cadmium
1228 in Seeds. *Mol Plant* **7**, 1455–1469 (2014).
- 1229 17. Selote, D., Samira, R., Matthiadis, A., Gillikin, J. W. & Long, T. A. Iron-Binding E3 Ligase
1230 Mediates Iron Response in Plants by Targeting Basic Helix-Loop-Helix Transcription
1231 Factors. *Plant Physiol.* **167**, 273–286 (2015).
- 1232 18. Kim, S. A. *et al.* Localization of iron in Arabidopsis seed requires the vacuolar membrane
1233 transporter VIT1. *Science* **314**, 1295–1298 (2006).
- 1234 19. Hohmann, U., Lau, K. & Hothorn, M. The Structural Basis of Ligand Perception and Signal
1235 Activation by Receptor Kinases. <https://doi.org/10.1146/annurev-arplant-042916-040957>
1236 <https://www.annualreviews.org/doi/abs/10.1146/annurev-arplant-042916-040957> (2017)
1237 doi:10.1146/annurev-arplant-042916-040957.
- 1238 20. Denyer, T. *et al.* Spatiotemporal Developmental Trajectories in the Arabidopsis Root
1239 Revealed Using High-Throughput Single-Cell RNA Sequencing. *Developmental Cell* **49**, 19
1240 (2019).
- 1241 21. Grison, M. S. *et al.* Plasma Membrane-Associated Receptor-like Kinases Relocalize to
1242 Plasmodesmata in Response to Osmotic Stress. *Plant Physiology* **181**, 142–160 (2019).
- 1243 22. Grison, M. S. *et al.* Specific Membrane Lipid Composition Is Important for Plasmodesmata
1244 Function in Arabidopsis. *The Plant Cell* **27**, 1228–1250 (2015).
- 1245 23. Sager, R. E. & Lee, J.-Y. Plasmodesmata at a glance. *J Cell Sci* **131**, (2018).

- 1246 24. Durrett, T. P., Gassmann, W. & Rogers, E. E. The FRD3-mediated efflux of citrate into the
1247 root vasculature is necessary for efficient iron translocation. *Plant Physiol* **144**, 197–205
1248 (2007).
- 1249 25. García, M. J. *et al.* Shoot to root communication is necessary to control the expression of
1250 iron-acquisition genes in Strategy I plants. *Planta* **237**, 65–75 (2013).
- 1251 26. Grillet, L., Lan, P., Li, W., Mokkaapati, G. & Schmidt, W. IRON MAN is a ubiquitous family
1252 of peptides that control iron transport in plants. *Nature Plants* **4**, 953–963 (2018).
- 1253 27. Khan, M. A. *et al.* Changes in iron availability in Arabidopsis are rapidly sensed in the leaf
1254 vasculature and impaired sensing leads to opposite transcriptional programs in leaves and
1255 roots. *Plant Cell Environ* **41**, 2263–2276 (2018).
- 1256 28. Kumar, R. K. *et al.* Iron-Nicotianamine Transporters Are Required for Proper Long Distance
1257 Iron Signaling. *Plant Physiology* **175**, 15 (2017).
- 1258 29. Vert, G. A., Briat, J.-F. & Curie, C. Dual Regulation of the Arabidopsis High-Affinity Root
1259 Iron Uptake System by Local and Long-Distance Signals. *Plant Physiol* **132**, 796–804
1260 (2003).
- 1261 30. Han, X. *et al.* Auxin-Callose-Mediated Plasmodesmal Gating Is Essential for Tropic Auxin
1262 Gradient Formation and Signaling. *Developmental Cell* **28**, 132–146 (2014).
- 1263 31. Huang, D. *et al.* Salicylic acid-mediated plasmodesmal closure via Remorin-dependent lipid
1264 organization. *PNAS* **116**, 21274–21284 (2019).
- 1265 32. Jaffe, M. J. & Leopold, A. C. Callose deposition during gravitropism of *Zea mays* and *Pisum*
1266 *sativum* and its inhibition by 2-deoxy-D-glucose. *Planta* **161**, 20–26 (1984).
- 1267 33. Shikanai, Y. *et al.* Callose Synthesis Suppresses Cell Death Induced by Low-Calcium
1268 Conditions in Leaves. *Plant Physiology* **182**, 2199–2212 (2020).

- 1269 34. Vatén, A. *et al.* Callose biosynthesis regulates symplastic trafficking during root
1270 development. *Dev Cell* **21**, 1144–1155 (2011).
- 1271 35. Benitez-Alfonso, Y. *et al.* Symplastic Intercellular Connectivity Regulates Lateral Root
1272 Patterning. *Developmental Cell* **26**, 136–147 (2013).
- 1273 36. Nicolas, W. J. *et al.* Architecture and permeability of post-cytokinesis plasmodesmata
1274 lacking cytoplasmic sleeves. *Nat Plants* **3**, 17082 (2017).
- 1275 37. Gerlitz, N., Gerum, R., Sauer, N. & Stadler, R. Photoinducible DRONPA-s: a new tool for
1276 investigating cell-cell connectivity. *Plant J* **94**, 751–766 (2018).
- 1277 38. Lee, J.-Y. *et al.* A Plasmodesmata-Localized Protein Mediates Crosstalk between Cell-to-
1278 Cell Communication and Innate Immunity in Arabidopsis. *The Plant Cell Online* **23**, 3353–
1279 3373 (2011).
- 1280 39. Sager, R. *et al.* Auxin-dependent control of a plasmodesmal regulator creates a negative
1281 feedback loop modulating lateral root emergence. *Nature Communications* **11**, 1–10 (2020).
- 1282 40. Millet, Y. A., Danna, C. H., Clay, N. K., Songnuan, W. & Simon, M. D. Innate Immune
1283 Responses Activated in Arabidopsis Roots by Microbe-Associated Molecular Patterns W
1284 OA. *The Plant Cell* **22**, 18 (2010).
- 1285 41. Stringlis, I. A. *et al.* Root transcriptional dynamics induced by beneficial rhizobacteria and
1286 microbial immune elicitors reveal signatures of adaptation to mutualists. *The Plant Journal*
1287 **93**, 166–180 (2018).
- 1288 42. Kreps, J. A. *et al.* Transcriptome Changes for Arabidopsis in Response to Salt, Osmotic, and
1289 Cold Stress. *Plant Physiol* **130**, 2129–2141 (2002).
- 1290 43. He, P. *et al.* Specific Bacterial Suppressors of MAMP Signaling Upstream of MAPKKK in
1291 Arabidopsis Innate Immunity. *Cell* **125**, 563–575 (2006).

- 1292 44. Hindt, M. N. *et al.* BRUTUS and its paralogs, BTS LIKE1 and BTS LIKE2, encode
1293 important negative regulators of the iron deficiency response in *Arabidopsis thaliana*.
1294 *Metallomics* **9**, 876–890 (2017).
- 1295 45. Satbhai, S. B. *et al.* Natural allelic variation of FRO2 modulates *Arabidopsis* root growth
1296 under iron deficiency. *Nature Communications* **8**, 15603 (2017).
- 1297 46. Belkhadir, Y. & Jaillais, Y. The molecular circuitry of brassinosteroid signaling. *New*
1298 *Phytologist* **206**, 522–540 (2015).
- 1299 47. Jaillais, Y. & Vert, G. Brassinosteroid signaling and BRI1 dynamics went underground.
1300 *Current Opinion in Plant Biology* **33**, 92–100 (2016).
- 1301 48. Tang, D., Wang, G. & Zhou, J.-M. Receptor Kinases in Plant-Pathogen Interactions: More
1302 Than Pattern Recognition. *The Plant Cell* **29**, 618–637 (2017).
- 1303 49. Benschop, J. J., Mohammed, S. & Slijper, M. Quantitative Phosphoproteomics of Early
1304 Elicitor Signaling in *Arabidopsis*. *Mol Cell Proteomics* **17** (2007).
- 1305 50. Cheval, C. *et al.* Chitin perception in plasmodesmata characterizes submembrane immune-
1306 signaling specificity in plants. *PNAS* **117**, 9621–9629 (2020).
- 1307 51. Lim, G.-H. *et al.* Plasmodesmata Localizing Proteins Regulate Transport and Signaling
1308 during Systemic Acquired Immunity in Plants. *Cell Host & Microbe* **19**, 541–549 (2016).
- 1309 52. Rutschow, H. L., Baskin, T. I. & Kramer, E. M. Regulation of Solute Flux through
1310 Plasmodesmata in the Root Meristem. *Plant Physiology* **155**, 1817–1826 (2011).
- 1311 53. Stonebloom, S. *et al.* Redox States of Plastids and Mitochondria Differentially Regulate
1312 Intercellular Transport via Plasmodesmata. *Plant Physiology* **158**, 190–199 (2012).

- 1313 54. Fichman, Y., Myers, R. J., Grant, D. G. & Mittler, R. Plasmodesmata-localized proteins and
1314 ROS orchestrate light-induced rapid systemic signaling in Arabidopsis. *Sci. Signal.* **14**,
1315 (2021).
- 1316 55. Smakowska-Luzan, E. *et al.* An extracellular network of Arabidopsis leucine-rich repeat
1317 receptor kinases. *Nature* **553**, 342–346 (2018).
- 1318 56. Haydon, M. J. *et al.* Vacuolar nicotianamine has critical and distinct roles under iron
1319 deficiency and for zinc sequestration in Arabidopsis. *Plant Cell* **24**, 724–737 (2012).
- 1320 57. Klatte, M. *et al.* The Analysis of Arabidopsis Nicotianamine Synthase Mutants Reveals
1321 Functions for Nicotianamine in Seed Iron Loading and Iron Deficiency Responses. *Plant*
1322 *Physiology* **150**, 257 (2009).
- 1323 58. Koen, E. *et al.* Arabidopsis thaliana nicotianamine synthase 4 is required for proper response
1324 to iron deficiency and to cadmium exposure. *Plant Sci* **209**, 1–11 (2013).
- 1325 59. Gruber, B. D., Giehl, R. F. H., Friedel, S. & von Wirén, N. Plasticity of the Arabidopsis Root
1326 System under Nutrient Deficiencies. *Plant Physiol.* **163**, 161–179 (2013).
- 1327 60. Alcázar, R. *et al.* Natural variation at Strubbelig Receptor Kinase 3 drives immune-triggered
1328 incompatibilities between *Arabidopsis thaliana* accessions. *Nature Genetics* **42**, 1135–1139
1329 (2010).
- 1330 61. Groen, S. C. *et al.* Pathogen-Triggered Ethylene Signaling Mediates Systemic-Induced
1331 Susceptibility to Herbivory in Arabidopsis[W]. *Plant Cell* **25**, 4755–4766 (2013).
- 1332 62. Higashi, K. *et al.* Modulation of defense signal transduction by flagellin-induced WRKY41
1333 transcription factor in Arabidopsis thaliana. *Mol Genet Genomics* **279**, 303–312 (2008).
- 1334 63. Lee, J.-Y. *et al.* A Plasmodesmata-Localized Protein Mediates Crosstalk between Cell-to-
1335 Cell Communication and Innate Immunity in Arabidopsis. *The Plant Cell* **23**, 22 (2011).

- 1336 64. Thomas, C. L., Bayer, E. M., Ritzenthaler, C., Fernandez-Calvino, L. & Maule, A. J.
1337 Specific Targeting of a Plasmodesmal Protein Affecting Cell-to-Cell Communication. *PLoS*
1338 *Biology* **6**, (2008).
- 1339 65. Cutler, S. R., Ehrhardt, D. W., Griffitts, J. S. & Somerville, C. R. Random GFP::cDNA
1340 fusions enable visualization of subcellular structures in cells of Arabidopsis at a high
1341 frequency. *PNAS* **97**, 3718–3723 (2000).
- 1342 66. Clough, S. J. & Bent, A. F. Floral dip: a simplified method for Agrobacterium-mediated
1343 transformation of Arabidopsis thaliana. *Plant J* **16**, 735–743 (1998).
- 1344 67. Slovak, R. *et al.* A Scalable Open-Source Pipeline for Large-Scale Root Phenotyping of
1345 Arabidopsis. *The Plant Cell* **26**, 2390–2403 (2014).
- 1346 68. Horton, M. W. *et al.* Genome-wide patterns of genetic variation in worldwide Arabidopsis
1347 thaliana accessions from the RegMap panel. *Nature Genetics* **44**, 212–216 (2012).
- 1348 69. Kang, H. M. *et al.* Efficient Control of Population Structure in Model Organism Association
1349 Mapping. *Genetics* **178**, 1709–1723 (2008).
- 1350 70. Seren, Ü. *et al.* GWAPP: A Web Application for Genome-Wide Association Mapping in
1351 Arabidopsis. *The Plant Cell* **24**, 4793–4805 (2012).
- 1352 71. Atwell, S. *et al.* Genome-wide association study of 107 phenotypes in Arabidopsis thaliana
1353 inbred lines. *Nature* **465**, 627–631 (2010).
- 1354 72. Brachi, B. *et al.* Linkage and Association Mapping of Arabidopsis thaliana Flowering Time
1355 in Nature. *PLOS Genetics* **6**, e1000940 (2010).
- 1356 73. Benjamini, Y. & Yekutieli, D. The control of the false discovery rate in multiple testing
1357 under dependency. *Ann. Statist.* **29**, 1165–1188 (2001).

- 1358 74. Kim, D. *et al.* TopHat2: accurate alignment of transcriptomes in the presence of insertions,
1359 deletions and gene fusions. *Genome Biology* **14**, R36 (2013).
- 1360 75. Anders, S., Pyl, P. T. & Huber, W. HTSeq—a Python framework to work with high-
1361 throughput sequencing data. *Bioinformatics* **31**, 166–169 (2014).
- 1362 76. Robinson, M. D., McCarthy, D. J. & Smyth, G. K. edgeR: a Bioconductor package for
1363 differential expression analysis of digital gene expression data. *Bioinformatics* **26**, 139–140
1364 (2009).
- 1365 77. Tian, T. *et al.* agriGO v2.0: a GO analysis toolkit for the agricultural community, 2017
1366 update. *Nucleic Acids Research* **45**, W122–W129 (2017).
- 1367 78. Boutté, Y. & Grebe, M. Immunocytochemical fluorescent in situ visualization of proteins in
1368 arabidopsis. *Methods in Molecular Biology* **1062**, 453–472 (2014).
- 1369 79. French, A. P. *et al.* Identifying biological landmarks using a novel cell measuring image
1370 analysis tool: Cell-o-Tape. *Plant Methods* **8**, 7 (2012).
- 1371 80. Schindelin, J. *et al.* Fiji: an open-source platform for biological-image analysis. *Nat Methods*
1372 **9**, 676–682 (2012).
- 1373 81. Bayle, V., Platre, M. P. & Jaillais, Y. Automatic Quantification of the Number of
1374 Intracellular Compartments in Arabidopsis thaliana Root Cells. *BIO-PROTOCOL* **7**, (2017).
- 1375 82. Gleave, A. P. A versatile binary vector system with a T-DNA organisational structure
1376 conducive to efficient integration of cloned DNA into the plant genome. *Plant Mol Biol* **20**,
1377 1203–1207 (1992).

1378
1379
1380
1381

Supplementary Files

This is a list of supplementary files associated with this preprint. Click to download.

- [20210630SUPPSpreadsheets.zip](#)
- [20210630SupplementalFigures.pdf](#)
- [20210630SUPPMOVIES.zip](#)